Technology Collaboration Programme
by iea

OES TASK 10 - Numerical Modelling of Wave Energy Converters

September 2024

PREPARED FOR:

International Energy Agency' Ocean Energy Systems Technology Collaboration Programme

PREPARED BY:

Kim Nielsen

OES OCEAN ENERGY SYSTEMS

IEA-OES Technology Collaboration Programme

IEA-OES is a Technology Collaboration Programme on Ocean Energy Systems within the International Energy Agency (IEA). Technology Collaboration Programmes are independent, international groups of experts that enable governments and industries from around the world to lead programmes and projects on a wide range of energy technologies and related issues.

This study is conducted as a part of the IEA-OES Task focused on Numerical Modelling of Wave Energy Converters.

Citation

IEA-OES (2024), Numerical Modelling of Wave Energy Converters. www.ocean-energy-systems.org

CONTENTS

1 Foreword 5
2 Introduction 6
3 Scope and Objectives 7
4 Numerical WEC modelling codes 7
4.1 Linear potential flow theory 8
4.2 Weakly Nonlinear Potential Flow Solution 8
4.3 Fully nonlinear potential flow theory 9
4.4 Computational Fluid Dynamics Models CFD 9
4.5 Five Prominent CFD Methods Explained 11
5 Verification and Validation of Numerical Models for WECs 13
5.1 Selection of WEC systems for modeling 13
5.2 Definition Of Metrics And Presentation Of Results 14
5.3 Regular waves 14
5.1 Irregular waves 16
5.1.1 Reference Wave Conditions at the Deployment Location 18
5.2 Analysis of the simulation results 20
6 Simulated Generic WEC Systems And Results 21
6.1 The Sphere 21
6.1.1 Forced Oscillation without damping. 25
6.1.2 Power production in regular waves including PTO damping. 25
6.2 The Heaving Float 28
6.2.1 Hydrodynamic coefficients 29
6.2.2 Specified test cases and results 29
6.3 The KRISO OWC system 32
6.3.1 The measurments on the OWC 33
6.4 The DTU OWC test case 39
6.4.1 The Experimental model 39
6.4.2 Case Specifications 41
6.4.3 Two-way damping 43
7 Conclusions 46
8 Future Work 47

8.1 Survival conditions & Design loads 47
8.2 Additional experimental test data 47
9 Annex with example calculations..48
9.1 Heaving sphere geometry 48
9.1.1 Hydrostatic..48
9.1.2 Hydrodynamic parameters 49
9.1.3 Decay test 51
9.1.4 Forced Oscillation 52
9.1.5 Energy Extraction and Optimal Damping 53
9.1.6 Calculation of Annual Energy Production 56
9.2 The DTU OWC example 57
9.2.1 Open Chamber Experiment 59
9.2.2 Time domain plot 60
9.2.3 Chamber with an orifice (Damped motion)..61
9.2.4 Linear damping 61
9.2.5 Linearized nonlinear damping. 62
9.2.6 Absorbed power and Capture width..63
10 Acknowledgements 64
11 References...65

1 FOREWORD

The work described in this report is the result of dedicated collaboration between 120 researchers from twenty countries. Professor Harry Bingham from DTU, Denmark, has kindly contributed with suggestions and improvements and assisted with proofreading this report on OES Task 10.

NREL in USA has been hosting the SharePoint server and their team of dedicated researchers has been the base for ensuring security and success, initiated by Bob Thresher.

The test cases described in this report were provided by institutions such as DTU, which contributed data for the DTU OWC test case. Sandia contributed with data of the heaving float test data from the Mask basin. AAU has provided dedicated experiments for the heaving sphere. KRISO in Republic of Korea has provided experimental data from a large fixed OWC model scale experiment.

A special thanks goes to the financial support provided by EUDP in Denmark, funding agencies in Sweden, the DOE in USA via NREL, Sandia and the TEAMER program, and finally the EU-funded WECANET for fostering collaboration.

Australia: UWA

Belgium: UGent

Croatia: University of Zagreb

Canada: Dynamic Systems Analysis, Cascadia Coast

China: National Ocean Technology Center, Guangzhou Institute of Energy Conversion, Shanghai Jiaotong University, Zhejiang Ocean University

Denmark: Ramboll, Aalborg University, DTU, Floating Power Plant (ES Consult observer)

France: Ecole Centrale de Nantes, Innosea

Germany: Forschungszentrum Küste

Hungary: Dept of Fluid Mechanics at Budapest University of Technology and Economics

Ireland: University College Cork, Wave Venture, Maynooth University

Italy: Politecnico di Torino

Japan: Saga University

Netherlands: MARIN, TU Delft

Norway: SINTEF Ocean, Dr. tech. Olav Olsen, EDRMedeso

Portugal: IST, WavEC and CENTEC

South Korea: KRISO

Spain: Tecnalia, Universidade de Vigo

Sweden: KTH, RISE and Chalmers University of Technology

Taiwan: National Yang Ming Chiao Tung University

UK: Plymouth University, Queen’s University Belfast; UEdin, EMEC

USA: NREL, Sandia National Laboratories, University of Hawaii, Glosten, Oregon State University

2 INTRODUCTION

In 2001 UK, Portugal, and Denmark initiated the OES Technology Collaboration Project under IEA. Today twenty-five different member states have joined. In 2016 Robert Thresher from NREL proposed the collaboration on numerical modelling of Wave Energy Converters (WEC's) "OES Task 10", based on good experiences from a similar task under IEA Wind. Within the OES group, interested teams and researchers from seventeen countries wanted to participate in Task 10. The EXCO decided to initiate Task 10 based on this great interest. This task offers a unique possibility to work together on common simulation tasks which enables and facilitates a better understanding of how wave energy conversion works. The photo in Figure 1 is from the first workshop at the Ibis Schiphol Hotel in Amsterdam.

This report presents results and lessons from the first years of the project, including two generic reference cases for numerical modelling of:

- Heaving WEC absorbers
- Oscillating Water Column (OWC) systems

The OES Webpage and the NREL share point site serves as a database for benchmark model case data and results for verification as well as code-to-code comparisons.

Figure 1The first international workshop September 2016 in Amsterdam, From the left: Imanuel Touzon, Sarah Thomsen, Carl-Erik Janson, Fabian Wendt, Massimiliano Leoni, Pilar Heres, Sarah Crowley, Edward Ransley, Kelley Ruehl and Kim Nielsen, (Tim Bunnik, Harry Bingham and Wanan Sheng only attended the first day)

3 SCOPE AND OBJECTIVES

The aim of the OES Task 10 is to gain experience and demonstrate the reliability and accuracy of the typical numerical codes and simulation tools used in wave energy research and development. The objective is to validate the models by comparing codes to codes and codes to experiments. The validation will focus on performance, loads, and responses related to the WEC in defined wave conditions. The objectives are the following:

1. To assess the accuracy and establish confidence in the use of numerical models.
2. To validate a ranges of existing computational modeling tools
3. To identify simulation methodologies leading to:
    - Reduced risk in technology development.
    - Improved device energy capture estimates (IEC TC 102)
    - Improved loading estimates
    - Reduced uncertainty in LCOE models
4. To establish future research and development needed to improve the computational tools and methods.

4 NUMERICAL WEC MODELLING CODES

The state of the art for the numerical modelling of WECs in general can be classified into three/four levels of refinement in terms of modelling the nonlinear hydrodynamics and including viscous effects:

1. Linear analysis in the frequency-domain.
2. Weakly nonlinear analysis in the time-domain.
3. Fully nonlinear analysis without wave breaking.
4. Computational Fluid Dynamics (CFD).

	Company	BEM	FNPF	CFD	W2Wmodel Time domain
Canada	DSA				Proteus Dean
Denmark	Floating PP AAU DTU Ramboll	 WAMIT WAMIT			WavePP
France	Innosea				INWave
Ireland	Wave Venture				
Netherlands	Marin	Difrac		ReFRESCO	TDM inhouse
Portugal	Wavec	x			W2WM
Spain	Technalia	x			TDM
Sweden	Chalmers SSPA KTH		Shipflow	OpenFOAM ReFRESCO FEniCS	
UK	QUB DNV	WAMIT		Openfoam	TDM Cummins Eqn.
USA	NREL, Sandia	x			WEC-Sim

Figure 2 Numerical codes used by the participants.

4.1 LINEAR POTENTIAL FLOW THEORY

The first level of analysis is of course to begin with a straightforward solution to the linearized problem in the frequency-domain, in which case the equations of motion reduce to:

$$\sum_{k=1}^{Nd}\left[-\omega^2(M_{jk}+A_{jk})+\mathrm{i}\omega\left(B_{jk}+B_{jk}^0\right)+C_{jk}+C_{jk}^0\right]\xi_k = X_j \qquad where\ \ j=1,2,\ldots..N_d$$

Where M_{jk}, A_{jk}, B_{jk} & C_{jk} are the linearized inertia, added mass, damping and hydrostatic restoring force coefficients for the WEC, while X_j, is the wave exiting force, B_{jk}^0& C_{jk}^0 are external damping and stiffness coefficients representing the mooring system and/or the PTO. This equation is dimensional, so the wave amplitude is part of X_j here. The body response is given by:

$$x_k(t) = \Re\left\{\xi_k e^{\mathrm{i}\omega t}\right\}$$

where ω is the incident wave frequency and N_d is the total number of degrees of freedom for the WEC. Here we allow for the possibility that the WEC has extended degrees of freedom beyond the normal six rigid-body modes to account for hinged or flexible structures and/or internal Oscillating Water Column chambers. The frequency domain response normalized by the incident wave amplitude is referred to as the Response Amplitude Operator (RAO).

The first group of numerical models use potential flow theory. Potential flow refers to a description of a fluid flow with no vorticity in it. Potential flow describes the velocity field as the gradient of a scalar function: the velocity potential. As a result, a potential flow is characterized by an irrotational velocity field, which is a valid approximation for several applications.

In the case of an incompressible flow the velocity potential satisfies Laplace's equation, and potential theory is applicable. However, potential flows also have been used to describe compressible flows and Hele-Shaw flows. The potential flow approach occurs in the modeling of both stationary as well as nonstationary flows.

4.2 WEAKLY NONLINEAR POTENTIAL FLOW SOLUTION

At this level, we assume that the radiation and diffraction waves generated by the WEC are of small amplitude relative to the wavelength and the water depth. There is a limit to the maximum ratio of a nonlinear to a linear term in the free-surface boundary conditions. We also assume that certain non-linear external forces can be applied to the body, without violating the original hydrodynamic assumptions. Under these assumptions, standard linear theory (here we can use WAMIT [1] or Nemoh [2]) can be used to approximate the radiation and diffraction interaction forces, while all other contributions remain fully nonlinear. In particular, the nonlinear hydrostatic and Froude-Krylov forces can be put into a particularly convenient form which depends only on the submerged volume of the WEC bounded by the incident wave elevation on the inside of the body.

Assuming that the incident wave is given by a known function or numerical solution, these terms are straightforward and computationally inexpensive to compute so that the total solution effort for this approach is not significantly larger than a pure linear solution. External mooring line loads and PTO forces are also included in a fully nonlinear manner.

WAMIT is a computer program based on the linear and second-order potential theory for analyzing floating or submerged bodies, in the presence of ocean waves. The boundary integral equation method (BIEM), also known as the panel method, is used to solve for the velocity potential and fluid pressure on the submerged surfaces of the bodies. Separate solutions are carried out simultaneously for the diffraction problem, giving the effects of incident waves on the body, and the radiation problems for each of the prescribed modes of motion of the bodies. These solutions are then used to obtain the relevant hydrodynamic parameters including added-mass and damping coefficients, exciting forces, response-amplitude operators (RAO's), the pressure and fluid velocity, and the mean drift forces and moments. The second-order module, Version 6S, provides complete second-order nonlinear quantities in addition.

WAMIT includes several unique options to facilitate its application in the most effective manner. In addition to the conventional low-order method, where the geometry is represented by small quadrilateral panels and the velocity potential is assumed constant on each panel, a powerful higher-order method is also available based on the representation of the potential by continuous B-splines and with a variety of options to define the geometry of the body surface approximately or exactly.

When multiple bodies are considered the hydrodynamic interactions between the bodies are included in the computations, without approximation. In addition to the conventional six degrees of rigid-body motion WAMIT also enables the user to define additional generalized modes to represent a wide variety of physical phenomena including hydroelasticity deformations, motions of hinged structures, various types of wave-energy converters, damping of gap and moonpool resonances, wavemakers, etc.

There exists a wealth of simulation tools based on the WNPF approximations, both commercial models – e.g. Orca flex [3], Ansys- Aqua [4], ProtuesDS [5] – as well as open-source models such as WEC-Sim [6], DTUMotionSimulator [7], FryDOM [8], MoodyMarine [9].

4.3 Fully nonlinear potential flow theory

Under the assumptions of a potential flow (i.e., an inviscid in irrotational motion), the mathematical description of the problem is simplified, and the resolution requirements are dramatically reduced. A single valued free-surface elevation (non-breaking waves) is also assumed which allows for high-order numerical approximations and increased computational efficiency. Capturing and re-griding the moving body and waterline to high-order accuracy is still very challenging however, and results using this method exist, i.e. ShipFlow [10].

4.4 Computational Fluid Dynamics Models CFD

Computational fluid dynamics models (CFD) solve the Navier-Stoke equations for either a single-phase or a two-phase fluid. According to reference (https://www.dive-solutions.de/blog/cfd-methods) Leonhard Euler and Joseph-Louis Lagrange, had quite differing views when it came to observing fluid flow. Euler wanted to observe the river while standing still. Lagrange, on the other hand, preferred to dive into the river and then look around himself while drifting with the current.

Eulerian methods utilize a static mesh to describe the domain, which the fluid passes through. The mesh typically does not change, and fluid fluxes are calculated on the cell faces. Since the mesh connectivity is unchanged, these cells and their neighbors stay the same throughout the simulation making differential calculations efficient and straightforward. The use of a pre-defined mesh means Eulerian methods can refine solution results in areas of high gradients and increase computational efficiency in areas of little interest. However, Eulerian methods can struggle with tracking material interfaces due to their fundamentally continuum representation of solution quantities, which are inherently discontinuous at these interfaces.

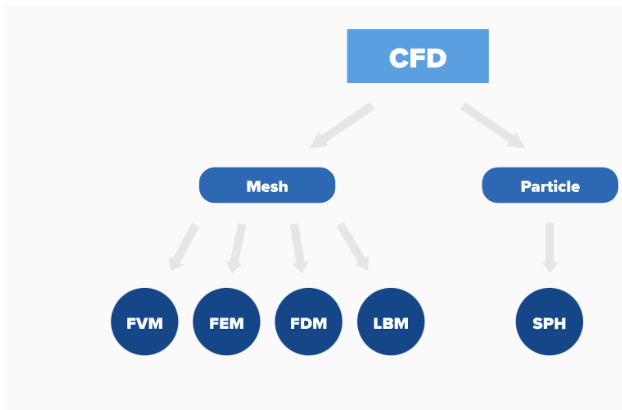

Figure 3 Illustration of the five prominent CFD methods

Lagrangian methods, on the other hand, do not use a mesh, but rather points which that can move around freely in space. Fluid motion is tracked directly on points that carry mass and volume, usually called particles. These particles are accelerated directly with fluid forces and define the motion of the flow. Their neighboring particles are changing constantly. While Lagrangian methods simplify interface and material tracking, gradient calculations become more expensive requiring continuous updating of neighbors and connectivity. Further, since the location of particles is determined by the fluid flow, the distribution of particles can be difficult to control, resulting in a scarcity of particles in the areas of interest and a clustering of particles in areas of little interest.

Arbitrary Lagrangian-Eulerian (ALE) methods have been developed as a compromise between these two approaches. In ALE methods, the mesh is allowed to transport with the fluid flow in a Lagrangian manner to better track interface motions, and Eulerian fluxes are calculated relative to the moving mesh velocity.

4.5 FIVE PROMINENT CFD METHODS EXPLAINED

1. Finite Difference Method (FDM)
2. Finite Volume Method (FVM)
3. Finite Element Method (FEM)
4. Lattice Boltzmann Method (LBM)
5. Smoothed Particle Hydrodynamics (SPH)

Mesh-based simulation approaches like the FDM, FVM and the FEM are used to accurately simulate fluid flows but struggle with multiphase flows, free surface flows and moving geometries due to their dependency on the mesh topology. This struggle is often based on increasingly complicated preprocessing steps and a bad computational performance due to costly adaptive remeshing algorithms. But let us be clear on that point: these methods are great to solve fluid flow problems without moving parts or even static boundaries. All methods presented have applications where they shine.

The Finite Volume Method is a Eulerian approach in which the flux into and out of a cell is calculated using the density, velocity and area at each face, and conservation of mass is strictly enforced at the cell level. However, for situations involving multiple materials within the same cell, such as air-water fluid interfaces, a reconstruction method (such as Volume of Fluid) is required to account for the multiple materials, and thus varying density, passing through a single face. FVM, FDM, FEM (also spectral and spectral element methods) can be applied in either an Eulerian, a Lagrangian or a Mixed Eulerian Lagrangian (MEL) framework.

Due to impressive performance increases, the LBM is already heavily used by engineers as an alternative to traditional mesh-based approaches. With the help of future research on LBM, this method surely will improve in the coming years and will continue to play a role in Computational Fluid Dynamics.

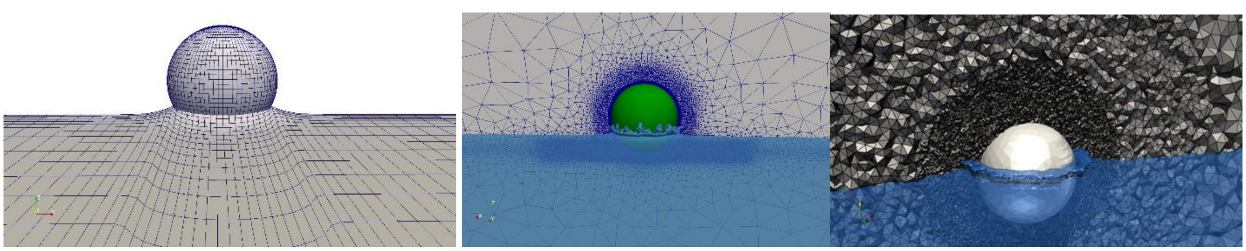

Figure 4 SHIPFLOW-Motions, LEMMA- ANANAS, Unicorn-FEniCS-HPC [WS3-Chalmers 2019-11-14]

SPH as a rising CFD method seems to be completely different from all other methods. The Lagrangian particle-based approach allows for the direct simulation of flows involving multiple materials without the need for pre-defined meshes or interface reconstruction. This enables completely new use cases, especially those that involve highly dynamical fluid flow, which would be very difficult to mesh with a static Eulerian-type grid, such as the oil flow in gearboxes, flows which rely heavily on tracking multiple mixing materials like tank sloshing or nozzle simulations. Improved fundamental understanding of the method and improved models will enable even more use cases and might allow for simulations of processes that cannot be captured with an existing simulation method in the future.

Sandia are using a classic Eulerian Finite Volume method with a Volume of Fluids (VOF) interface reconstruction with a static mesh, refined where we expect the interface to land, and track an "alpha" scalar which represents the percentage of water vs air in each cell – usually 1 or 0, but somewhere in the middle at the interface.

NREL is using a Lagrangian Smoothed Particle Hydrodynamics method, which tracks water particles ignoring the air. This means the interface does not need to be approximated, a surface can just be drawn over the top of the particles.

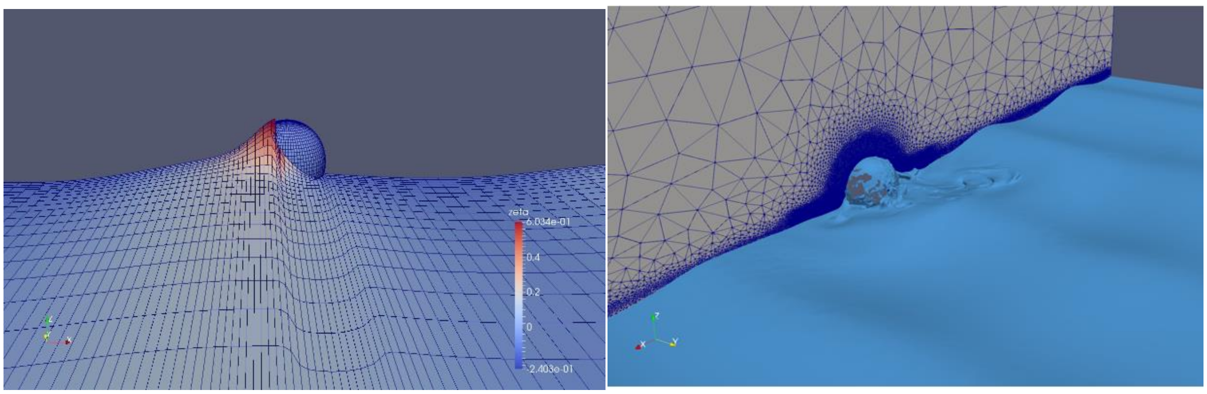

Figure 5 SHIPFLOW-Motions and LEMMA-ANANAS visualizations of simulations

5 VERIFICATION AND VALIDATION OF NUMERICAL MODELS FOR WECS

5.1 SELECTION OF WEC SYSTEMS FOR MODELING

The group had to decide what kind of wave energy converter to model. There are so many diverse types of Wave Energy Converter systems. The coordinator of the IEA Wind TCP task 30 [11] advised and suggested to start simple. The heaving sphere, for which exact analytical results in for the linear hydrodynamic coefficients and RAO are available, provides a simple case. As a test case, it resembles the archetype of heaving bottom referenced wave energy converters – typically known as point absorbers, circled in red on the Figure 6 below.

The second WEC archetype was the oscillating water column OWC type of WEC device. The choice to conduct simulation of an OWC wave energy converter, would in addition include modelling the extraction of power from the air chamber. The OWC type of Wave energy converter is the oldest, and the most advanced concept for exploiting ocean wave energy. In the 1800's the first OWCs were whistling, and later electric, navigational buoys. Shore-mounted installations have successfully contributed power to the electric grid, and the OE buoy is an example of floating OWC launched and assessed in Hawaii. More recently, Korea has developed innovative designs for breakwater mounted OWCs. The possible combinations of fixed or floating, point absorbers, terminators, attenuators, single column and multi columns are almost endless.

As a result, four different test cases have been chosen for comparing numerical results, "the heaving sphere" and "the Mask Basin float", "the KRISO OWC", and "the DTU OWC" test case. The results are summarized in section 6. The work on refining the test cases and experimental data sets is ongoing with focus on simulation of both OWC systems and heaving WEC devices, representing two specific WEC archetypes.

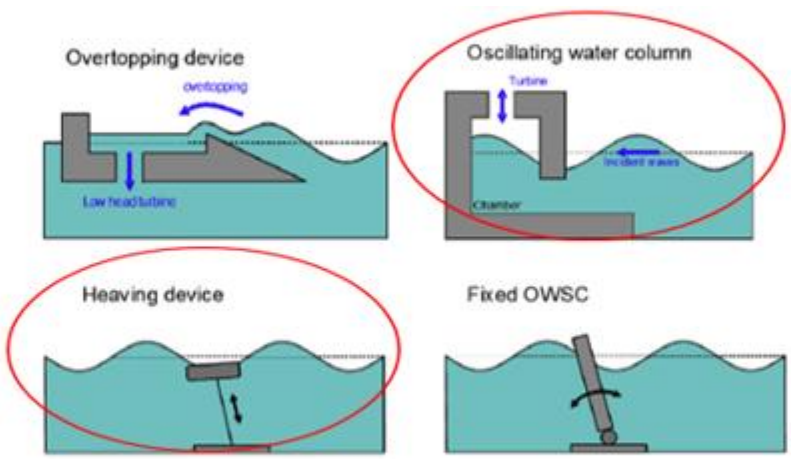

Figure 6 Illustration of four archetypes of wave energy device and the focus for OES Task 10 [A BABARIT 2015]

5.2 DEFINITION OF METRICS AND PRESENTATION OF RESULTS

To verify and compare analytical, experimental, and numerical results, the coordination group suggested the following metrics:

- Device loads, position, velocity, and acceleration
- Wave input
- Absorbed wave power.
- Measurement and simulation accuracy
- Repeatability and reproducibility of measurements

The coordination group also provided a template with specified time steps and labelled columns as shown in Table 1 below, for submitting the time series of simulation results for comparison.

Table 1Output format description

Colum	Description
1.	Time [s]
2.	Wave elevation [m]
3.	Heave response [m]
4.	Force on sphere in Heave at CG [N]
5.	Force on sphere in Surge at CG [N]
6.	Pitching Moment at CG [N]
7.	PTO force for optimal C_{PTO} cases [N]
8.	Power output for optimal C_{PTO} cases [W]

5.3 REGULAR WAVES

The participants calculate the WEC response amplitude operators (RAOs) using regular harmonic waves (cosine) over a range of specified wave periods. The choice of wave height will influence the wave steepness ($S = H/gT^2$). As illustrated in Figure 7, increasing wave steepness implies an increasing importance of nonlinear effects and a corresponding need to apply higher-order wave theory to achieve good accuracy. In addition, the response of the WEC at resonance, can result in large amplitudes and consequently, the nonlinear wave forces on the floating body become significant.

In deep water, the steepness becomes the ratio between the wave height and the deepwater wavelength λ, which is proportional to the wave period squared:

$$\lambda = \frac{gT^2}{2\pi}$$

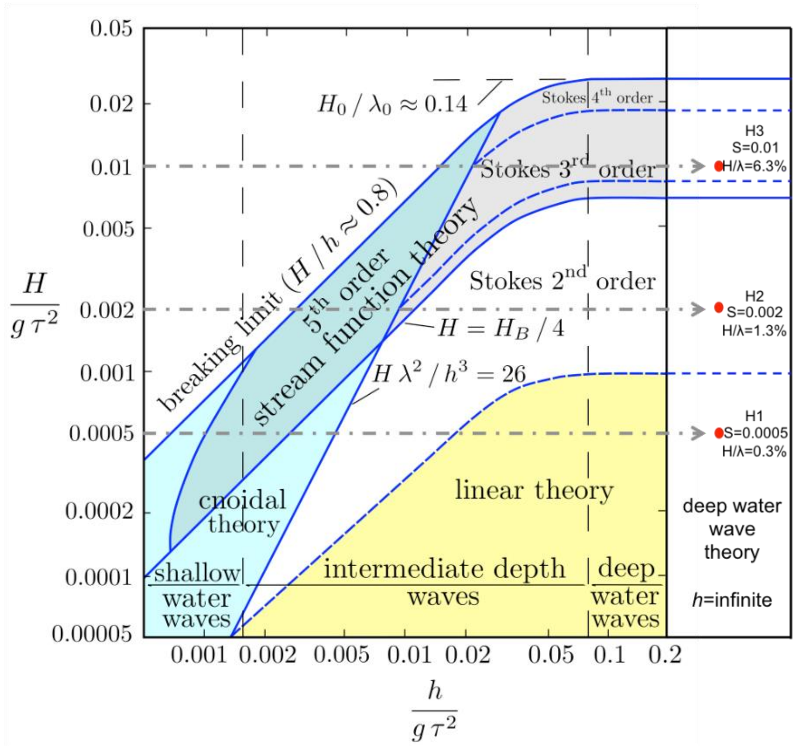

Figure 7 Validity of wave theories and analyzed wave states

The typical wave periods of interest in for wave power are shown in the table below, one can see that the wave period ranges from 3 – 11 sec. (wavelength range from 14 to 188 meter). Typically, ocean swell waves that have traveled out of a wind generation area will have a small steepness – whereas wind waves under generation will grow to be steeper and often reach the breaking limit H/λ ≈ 0,14 (also shown on the figure above). The small steepness column indicated by wave height H1, (S = 0.0005) are well-described by linear theory, while columns and H2 (S = 0.002) are covered by weakly nonlinear 2nd order theory and H3 (S=0.01). (H/λ = 6.3%) to 3rd- order nonlinear theory.

The simulation validations will be both more challenging and enlightening for steeper waves and it was later adapted to include wave steepness H/λ = 2.5% and H/λ = 4% shown in the last columns.

Table 2 Regular wave periods and heights recommended (in full scale).

T [sec]	f [Hz] 1/T	λ [m] Inf. deep	H1 [m] S = 0.0005	H2 [m] S = 0.002	H3 [m] S = 0.01	H4 [m] H/λ = 2.5%	H5 [m] H/λ = 4%
3.0	0.333	14.0	0.04	0.18	0.88	0,35	0,56
4.0	0.250	24.9	0.08	0.31	1.50	0,62	1,00
5.0	0.200	39.0	0.12	0.49	2.45	0,98	1,56
6.0	0.167	56.2	0.17	0.71	3.53	1,40	2,25
7.0	0.143	76.4	0.24	0.96	4.81	1,91	3,06
8.0	0.125	99.8	0.31	1.26	6.28	2,50	3,99
9.0	0.111	126.4	0.40	1.59	7.95	3,16	5,05
10.0	0.100	156.0	0.49	1.96	9.81	3,90	6,24
11.0	0.091	188.8	0.59	2.37	4,72	7,55	

5.1 IRREGULAR WAVES

Waves on the sea surface are irregular in nature. Large waves, small waves, short waves, and long waves follow each other, overtake and break. If a storm suddenly passes an ocean area, the sea will be set in movement the waves froths with foam while increasing in size. Depending on the speed of the wind and the available fetch at the point of observation the waves will grow to a certain size. When fully grown the crest of the waves will pass with a speed like that of the wind.

The waves will spread in different directions and are therefore not unendingly long crested, but their mean direction will follow the direction of the wind. When the waves move out of the wind-affected area they will travel long distances as swells with long crests.

The waves at a location change only slowly within periods of one to three hours and one speaks of a stationary prevailing sea condition (with a specific short-term distribution of waves).

The sea condition is often described by the significant wave height H_s and a wave period – the average wave period T_z if the wave train is analyzed statistically or the energy period T_e if the spectrum of the sea condition has been measured.

The irregular sea can be described using a Brettschneider spectrum with the significant wave height H_s and peak period T_p as input [12]. The peak period T_p is the period where there is most energy in the spectrum. The significant wave height is approximately the average wave height of the 1/3 largest waves. The Brettschneider spectrum expressed represented as a function of the wave frequency is:

$$S(f) = \frac{A}{(f)^5} \exp\left[\frac{-B}{(f)^4}\right]$$

where:

$$A = \frac{5}{16} H_s^{\,2} \left(\frac{1}{T_p}\right)^4 \qquad \text{and} \qquad B = \frac{5}{4}\left(\frac{1}{T_p}\right)^4$$

The spectral moments are defined as:

$$m_i = \int_0^\infty f^i S(f) df$$

The significant wave height $H_s = H_{mo}$ can be derived from moment m_0 of the spectrum as:

$$H_{m0} = 4\sqrt{m_0} \ \ [meter]$$

The average wave period $T_z = T_{02}$ can be found from the spectrum moment m_0 and m_2

$$T_{02} = \sqrt{\frac{m_0}{m_2}} \ \ [sec]$$

The Energy Period Te has been introduced in connection with wave power studies as it contains information on the integral m_{-1} proportional to the wave energy flux (14) of the sea state. The moment m_{-1} strongly depends on the lower frequency parts of the spectrum (longer wave periods). The energy period is defined as:

$$T_e = \frac{m_{-1}}{m_0} \quad [sec]$$

$$T_e \approx 1.2\, T_{02} \quad [sec]$$

The wave energy flux of wave power is average power in Watts per metre wave crest, it describes the average wave power that passes through a one-metre-wide fictive vertical surface perpendicular to the direction of propagation and extending to the seabed. In deep water the wave energy flux can be calculated by integrating the spectrum wave components times the wave group velocity $c_g(f)$:

$$P_W = \rho g \int_0^\infty S(f)\, c_g(f)\, df$$

$$c_g(f) = \frac{g}{4\pi f}$$

$$P_w = \rho g^2 \frac{1}{4\pi} \int_0^\infty S(f) \frac{1}{f} df = \rho g^2 \frac{1}{4\pi} m_{-1}$$

The Wave Power expressed in terms of H_s and T_e is:

$$P_w = \frac{\rho g^2}{64\pi} H_s^2 T_e$$

To calculate the mean power production in a defined spectrum using the measured or calculated capture length CL(f) in regular waves, we compute:

$$P_{abs} = \rho g \int_0^\infty S(f) c_g(f)\, CL(f) df$$

The capture length, CL(f), in regular waves is given by:

$$CL(f) = \frac{P(f)}{\frac{1}{2} \rho g A^2 c_g(f)}$$

Where $P(f)$ is the power absorbed in regular waves of period *f=1/T* with amplitude *A*. Further elaboration in relation to spectral presentation as a function of the period wave period T is given in Section 9.

5.1.1 <u>Reference Wave Conditions at the Deployment Location</u>

The time span considered in connection with the long-term distribution of wave conditions is on the order of the lifetime of the structure. The distribution of the sea conditions can be shown in a scatter diagram in terms of number per thousand observations (or how many hours per year) different combinations H_s of and T_z or T_e prevails over the year.

The scatter of numbers in each combination of H_s and T_e depends on the position in the ocean, the water depth, the wind climate, and the fetch and size of the ocean area. In a sheltered shallow water area, waves will rarely exceed H_s = 1.5 m. In the North Atlantic Ocean in deep water, significant wave heights exceeding H_s = 10 m might prevail during extreme wind conditions.

In general, there is an upper limit for the significant wave height as a function of the average wave period. This is because if waves get too steep, they break and re-distribute their energy. The limit for the significant wave height expressed in terms of the average period is estimated to be:

$$H_s < 0{,}07{T_e}^2$$

A generic study of the wave conditions at selected location in Europe was caried out as Annex II in 2010 [13]. A scatter tables of H_s and T_e as shown in Table 3 is presented for each location. Each cell represents an interval of 1 second for the energy period T_e and 0,5 meter for the significant wave height H_s is. The value in each cell shows the relative frequency of occurrence (parts per thousand) of the respective combination (H_s, T_e).

Table 3 Scatter table of wave condition, North Sea location in Annex II 2010 [13]

Hs \ Te	2,5	3,5	4,5	5,5	6,5	7,5	8,5	9,5	10,5	11,5	12,5	13,5	14,5	15,5	Sum	Acc	Te ave	dP
0,25		4	14	7	4	2									31	31	5,05	0,00
0,75		9	64	56	23	10	6	2	1						171	202	5,45	0,26
1,25			38	93	41	15	7	2	1						197	399	5,84	0,89
1,75			2	75	64	21	9	4	1						176	575	6,36	1,69
2,25				23	76	25	8	4	1	0					137	712	6,75	2,31
2,75				2	49	32	10	4	1	1					99	811	7,22	2,67
3,25					19	38	9	3	1	0	0				70	881	7,49	2,73
3,75					3	27	12	2	1	0	0				45	926	7,86	2,45
4,25						13	12	2	0	0					27	953	8,09	1,95
4,75						3	11	2	1	0	0				17	970	8,56	1,62
5,25						1	8	3	0	0	0				12	982	8,67	1,41
5,75							3	3	1	0	0				7	989	9,21	1,05
6,25							1	2	1	0	0				4	993	9,50	0,73
6,75								1	1						2	995	10,00	0,45
7,25								1	0	0					1	996	9,50	0,25
7,75																		
	0	13	118	256	279	187	96	35	11	1	0	0	0	0	996			20,47

For each row of H_s, the average energy period is calculated and shown in the column (Te ave) this value is the most likely energy period associated with the row of value of H_s. Central values of H_s and T_e for each bin are used assuming an even distribution within each bin.

The probability of each row of H_s is shown in the column (sum), the accumulated probability in column (Acc) and the power contribution from each row of Hs shown in column (dP).

Summing up the power contributions (dP) in column (dP) for each row gives an estimate of the power resource in this case 20.47 kW/m at the site is obtained as a sum over the column.

A plot of the average energy period T_e as a function of H_s is shown below at the corresponding scatter table. A trend line giving the best linear fit between the plotted points is shown.

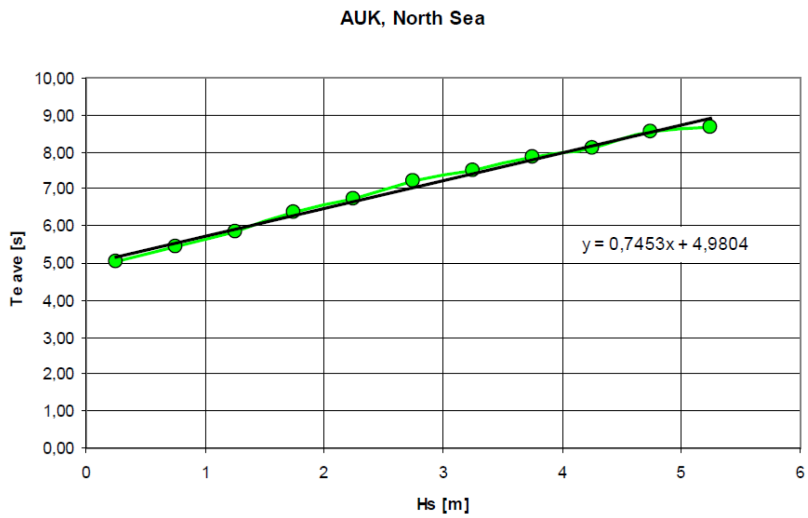

Figure 8 Plot of the relationship between Hs and the average energy period Te ave

This methodology, using a linear relationship between H_s and T_e for a specific ocean location provides a simple method to analyze the data. The relation between T_e and H_s in the North Sea is:

$$T_e(H_s) = 0.75H_s + 4.98$$

The annual energy production from a WEC can be calculated using the simplified methodology provided by Nielsen & Pontes (2010). The power production in each of the six sea states with H_s specified in Table 4 should be calculated and multiplied with the hours that each sea state occurs and summed up to calculate an estimate of the annual energy production.

The North Sea AUK with an average wave power resource of 20 kW/m is used as an example.

Table 4 Five basic sea states for the location North Sea (AUK) [13]

H_s [m]	1m	2m	3m	4m	5m	>5,5m	Total
Energy period T_e [sec]	5,73	6,47	7,22	7,96	8,71	>9,08	
Hours per year	3224	2742	1480	631	254	123	8725
Energy [kWh/m/year]	10233	35737	48198	39296	27097	22153	182757

5.2 ANALYSIS OF THE SIMULATION RESULTS

The simulation results of waves, response, loads, power, and pressure presented as a function of time was post processed and compared with experimental data in a side-by-side fashion. Simple comparison plots that compare and evaluate the numerical simulation results in a side-by-side fashion can illustrate a difference in the different type of models.

The procedures for data submission, analysis, and comparison, were developed over time since the first test case with the floating sphere was selected. This part of the project included systematic procedures for uploading of results as well as downloading for post processing.

Workshops have been a helpful tool in reaching the results, with financial support from OES and from the pan-European Network for Marine Renewable Energy with a Focus on Wave Energy WECANET [13].

Figure 9 Workshop discussion of results face to face 2020 supported by WECANET [14].

6 SIMULATED GENERIC WEC SYSTEMS AND RESULTS

In this chapter we will describe the test cases adapted for the OES Task 10 study on verification and validation of numerical models. For the four test cases we will summarise and present the results obtained during the project period.

6.1 THE SPHERE

To engage the wide range of interested parties that wanted to participate in the numerical task the coordinator of the IEA Wind TCP Task 30 suggested the OES Task 10 group to start simple. To start by identifying a suitable analytical model of a wave energy converter for verification of the numerical models.

The heaving sphere for which exact analytical results in terms of hydrodynamic coefficients and RAOs was available was a simple case. AAU has since the first tests elaborated on this case to also include dedicated experimental data for verification and validation for specified wave cases and the development and integration of an experimental PTO is ongoing development.

The heaving sphere can in a generic way illustrate the principle of a point absorber, such as initially developed and tested by Budal and Falnes [15] in Norway, and later further developed by CorePower Ocean [16] as shown on Figure 10 below.

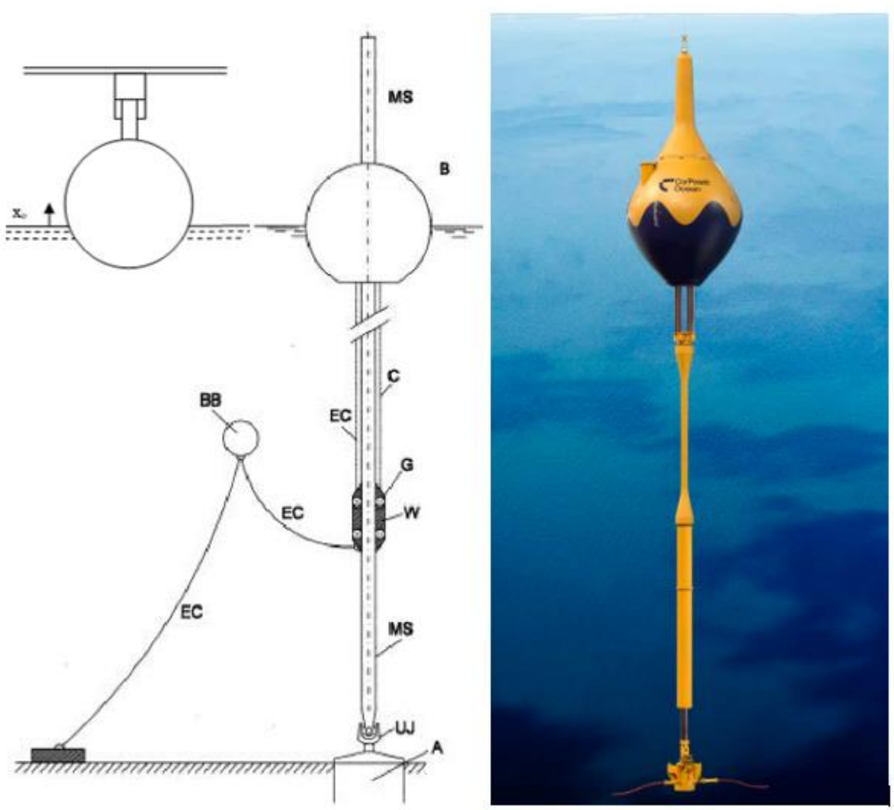

Figure 10 The Heaving sphere representing a generic point absorber WEC.

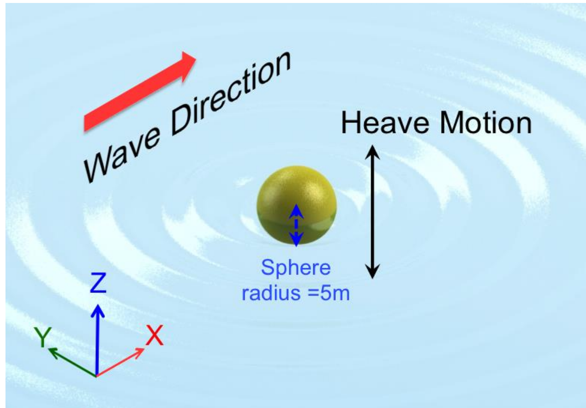

Figure 11 First test case was the Heaving Sphere

The initial numerical experiment was to compare the numerical and analytical results of the hydrodynamic coefficients and those calculated using modern tools such as WAMIT [1].

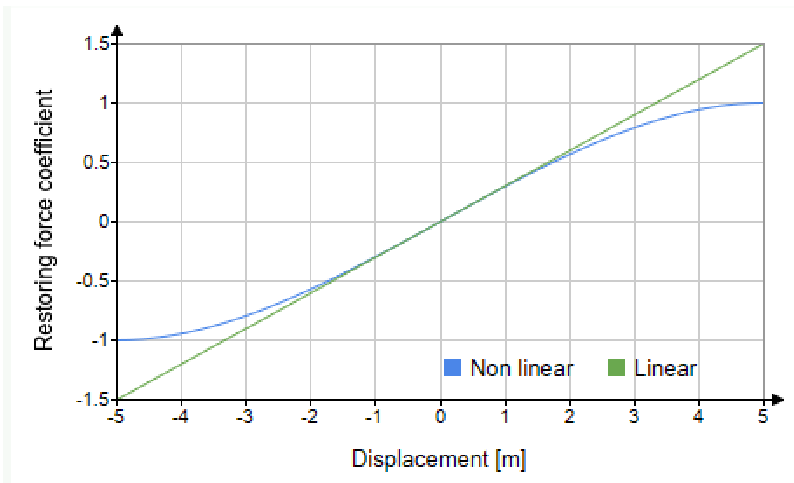

Figure 12 Comparison between the linear and non-linear variation of hydrostatic force with vertical displacement

The group was asked to simulate the heave decay experiment for the heaving sphere with no waves just a given initial offset. The simulations were caried out in full scale for the 10-meter diameter sphere. The comparison between the different type of models used by the teams all shows good agreement, for the initial elevation of 1 meter up.

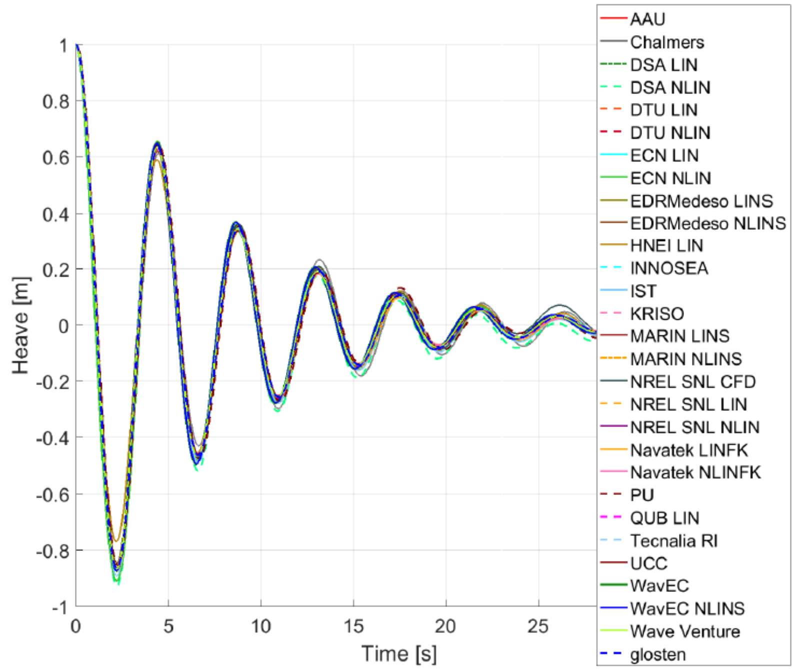

Figure 13 Plot of the free decay experiment theory.

The decay test case with initial elevation of 5 meter (float almost out of water) however clearly showed that the different models using different assumptions and simplifications now also showed different results as can be seen on the plot on Figure 14 below.

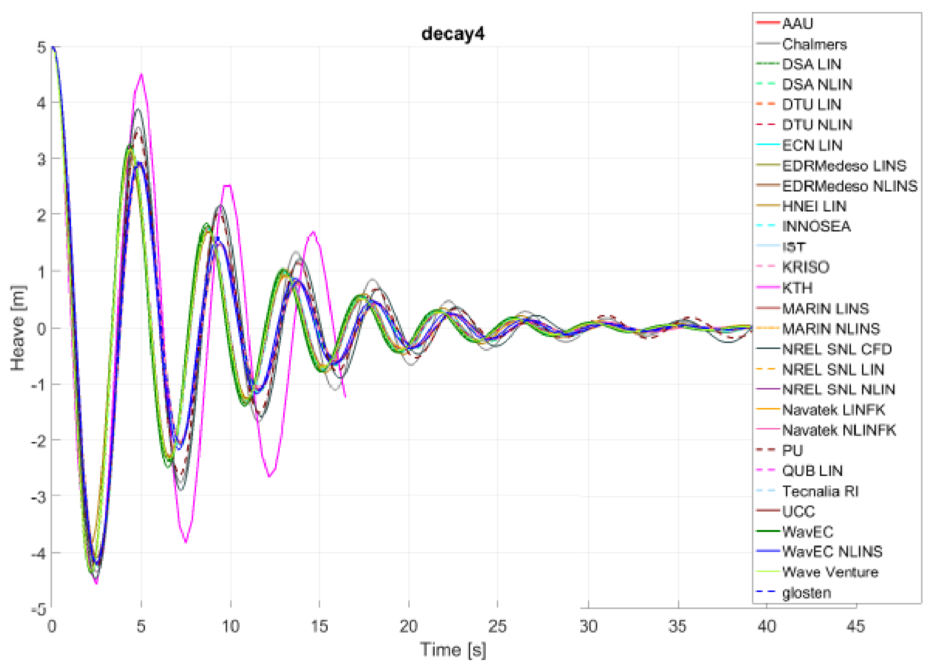

Figure 14 of the free decay experiment theory .

The results are grouped according to their theoretical complexity.

1. Purely linear codes,

The linear models assume very small displacements and therefore a constant water plain area independent of the displacement. These models agree well for small amplitudes.

2. Codes with weak nonlinearities.

The weakly nonlinear codes capture this geometric nonlinearity of the buoyancy force as a function of the displacement. These models consider the instantaneous body position for calculating the hydrostatic restoring force. This is not captured by the completely linear models.

3. Codes with strong nonlinearities.

These codes predict a larger motion amplitude compared to the previous group. The codes with strong nonlinearities, can capture higher order wave radiation effects, which are largely influenced by the instantaneous sphere cross section area at the water surface.

4. CFD models. In addition,

CFD solution predicts breaking of the radiated wave around the sphere during the first oscillation, this effect can only be captured by CFD solutions. However due to the round shape of the sphere the effect of fluid viscosity plays a relatively small role in the analyzed scenario, which tends to give a relatively good agreement with weakly non-linear results.

A complete overview of the results is given in the OES task 10 papers [17] [18] and [19]. To further evaluate the results, dedicated experiments are being developed by AAU as shown on the figure below and described in [25] with link https://doi.org/10.3390/en14020269 .

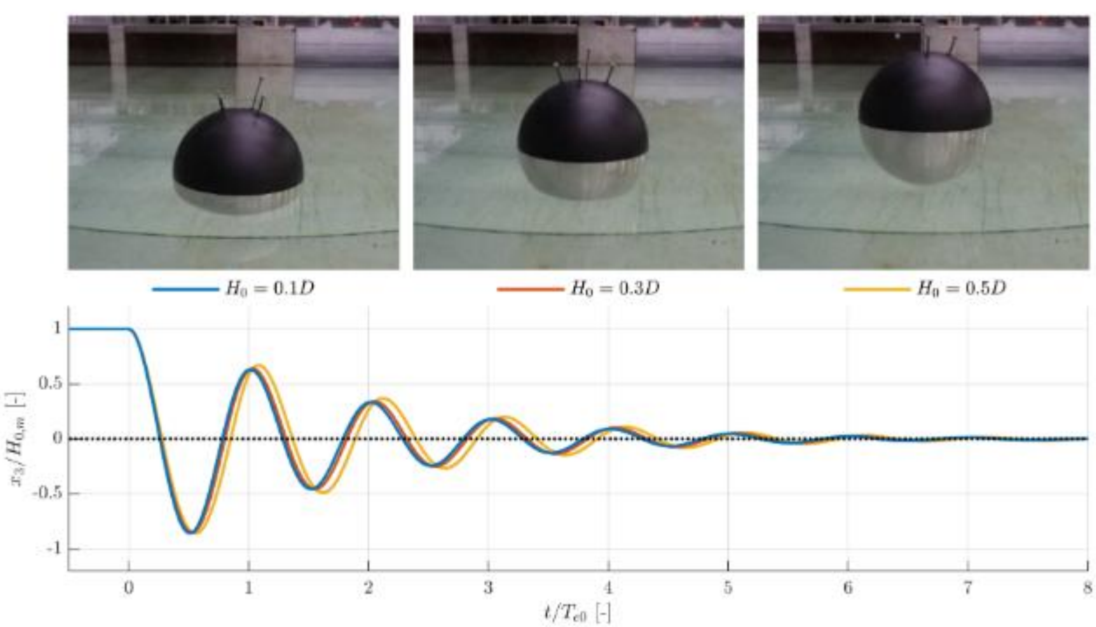

Figure 15 Dedicated experiment for the heaving sphere

6.1.1 Forced Oscillation without damping.

All models seem to agree well when simulating the free heave response for the case (without PTO damping), as seen in Figure 16 This outcome is likely because in long waves the free-floating sphere behaves more as a wave follower, which mitigates nonlinearities induced by changes in relative position between the instantaneous free-water surface and the heaving sphere and therefore also very small viscous effects [17].

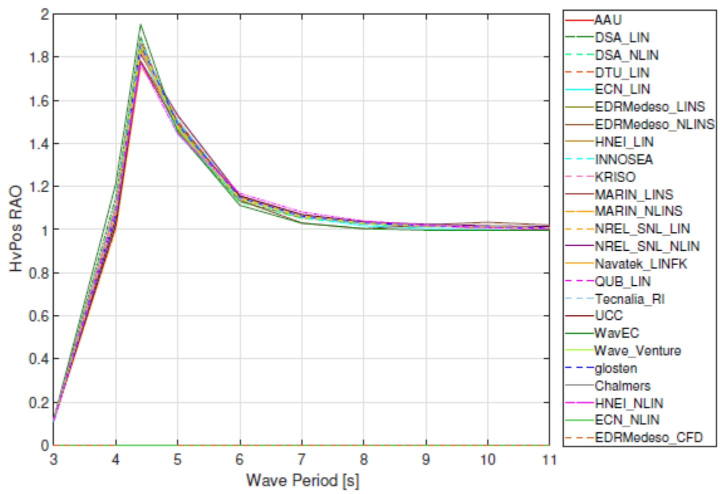

Figure 16 Heave RAO comparison no damping largest steepness S=0.01

6.1.2 Power production in regular waves including PTO damping.

However, when the PTO damping is included the heave response will reduce. The calculation models that include geometric nonlinearities, showed an increased damping in longer and higher waves compared to the linear models.

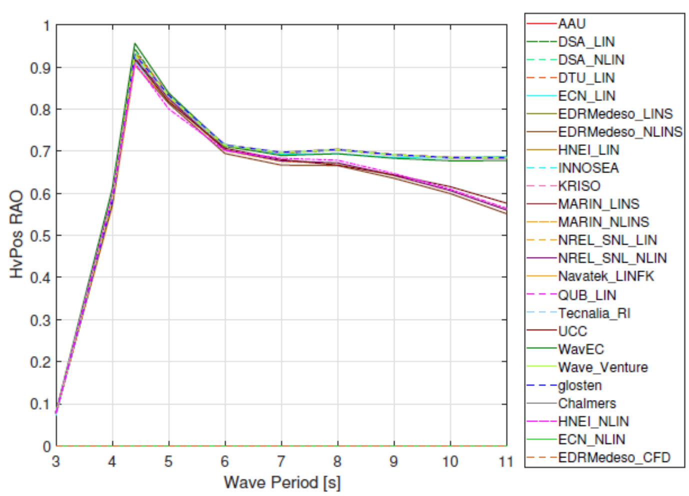

Figure 17 Heave response including optimum PTO damping [17]

As a result, the absorbed power predicted by the non-linear models are lower compared to the calculations using linear models, for the longer and larger waves as shown Figure 18 below.

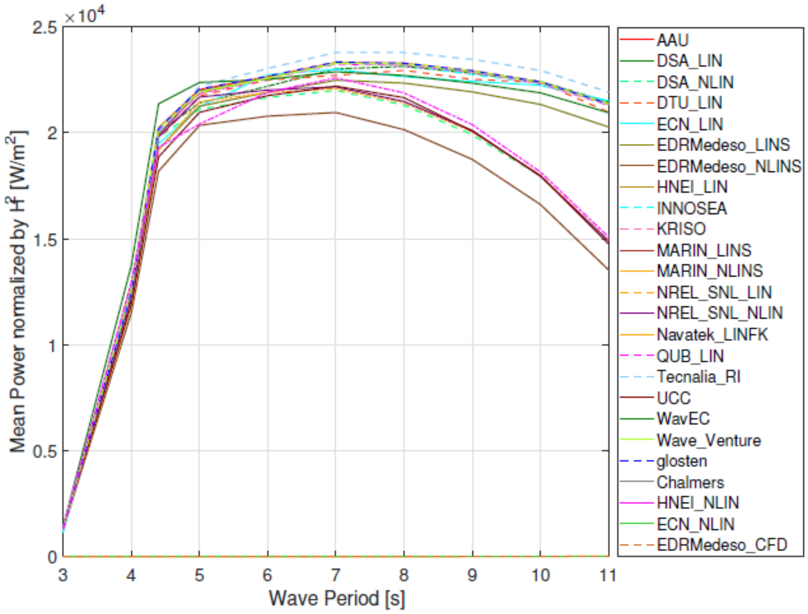

Figure 18 Mean power normalized by the square of the wave height, S = 0:01, optimum PTO damping.

Finally, the average power production in irregular waves was calculated using specified distribution of irregular waves modelled using Brettschneider spectrums.

Table 5 Selected sea states (in full scale) and corresponding weighing

1	2	3	4	5	6	7
Wave #	**Tp (s)**	**Hs (m)**	**Weight (%)**	**Linear Damping Without Additional Spring (Ns/m)**	**Additional Linear Spring Stiffness (N/m)**	**Linear Damping With Spring (N/m)**
IWS 1	6.647	1	36.951	4.248490e+05	-3.762340e+05	8.647091e+04
IWS 2	7.505	2	31.427	5.584053e+05	-4.506551e+05	7.543009e+04
IWS 3	8.375	3	16.963	6.906004e+05	-5.069603e+05	6.425628e+04
IWS 4	9.234	4	7.232	8.190450e+05	-5.497978e+05	5.444402e+04
IWS 5	10.104	5	2.911	9.473561e+05	-5.840240e+05	4.584260e+04
IWS 6	11.136	6.1	1.410	1.096585e+06	-6.154603e+05	3.740378e+04

The damping parameter is assumed constant in each irregular sea state, and larger sea states with longer wave periods require more damping to extract the most energy. The optimal damping used corresponds to the optimal damping for a regular wave with the period equal to the peak period of the spectrum $T=T_p$.

The annual average absorbed power based on these simulations from the OES Task 10 team is presented in Table 6. The annual average absorbed power estimated showed an average of 47,9 kW based on the simulations from the 12 partners, with a maximum of 49,3 kW and a minimum of 46,4 kW and standard deviation 1.07 kW. The difference in results is in most cases due to truncation of the time series.

The float response amplitude in these irregular wave cases, is noted to be less than 4 meters, which is realistic.

Table 6 The AAP reported by the participants.

OES Tas 10 Participant	AAP [kW]
#1 NREL/SANDIA	47.7
#2 Technalia	48.4
#3 KRISO	48.7
#4 Wave EC	46.4
#5 Université College Cork	47.1
#6 Aalborg University	47.0
#7 Innocea	47.7
#8 EC Nantes	46.4
#9 Wave Venture	46.9
#10 Dynamic System Analysis	49.3
#11 Technical University of Denmark	49.3
#12 Floating Power Plant	49.3

6.2 THE HEAVING FLOAT

As a second test case the OES Task 10 group wanted to use existing experimental data for verification. The team reviewed existing experimental data from Wave Energy Converters made available for comparison and validation of numerical simulations. What is a good experimental setup? How important is the scale, the number of degrees of freedom and how about mooring forces? If moving from a heaving bottom mounted WEC, should it be a hinged WEC or – a rotating vane, moving vertical, horizontally, aligned, or perpendicular to the direction of wave propagation, and what type of PTO? Figure 19 below shows the model cases considered.

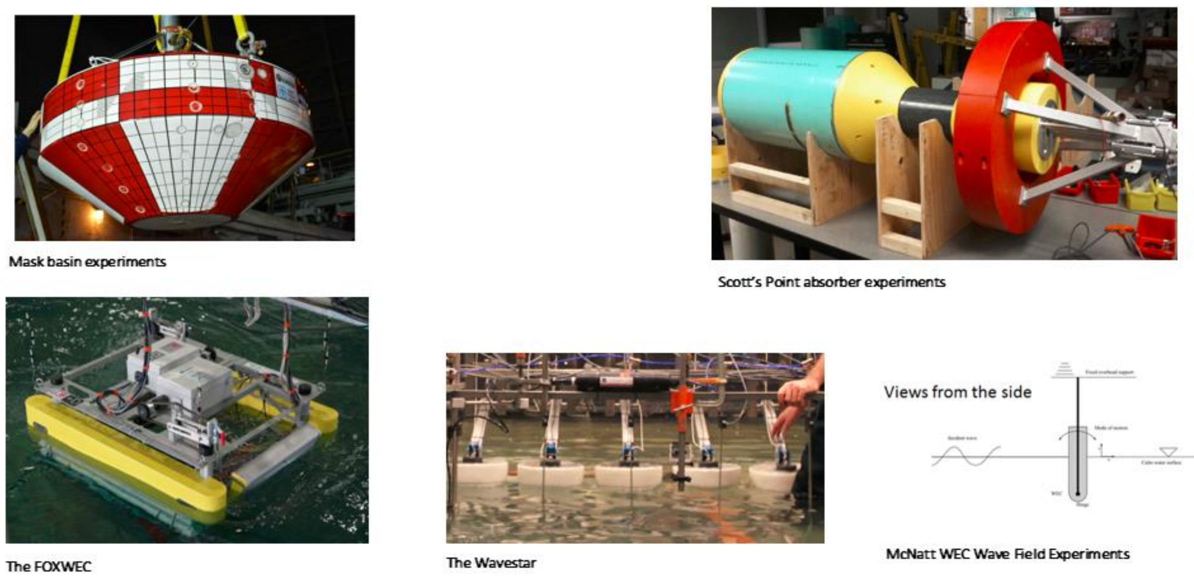

Figure 19 Selecting a reference case between a limited number of existing experimental test cases.

The final choice was to use the experimental data from Sandia National Laboratories carried out as part of testing campaign in the US Mask basin, as described in [21]. It was a heaving float case again, but the geometry of the cross section of the float was different as shown in Figure 20 having a surface-piercing body with a cylinder on top and a conical frustum on the bottom. The testing was carried out at scale 1:17.

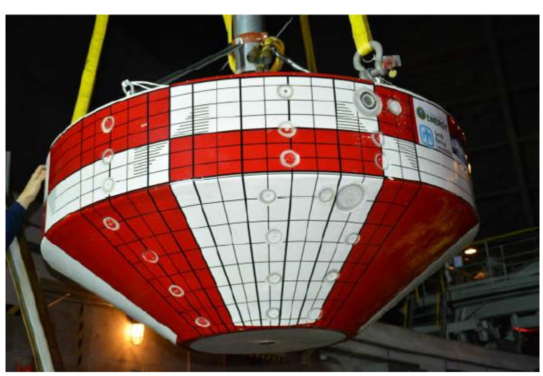

Figure 20 Mask basin test of heaving float

Parameter	Value
Radius	0.88 m
Draft	0.53m
Mass (incl. slider)	858 kg
Displacement	0.858 m^3
Mass (float only)	660 kg
Water Depth	6.1 m
Water Density	1000.0 kg/m^3

Resonance period:

$T_0 = 1.5385$ s

(equal to 0.65 Hz)

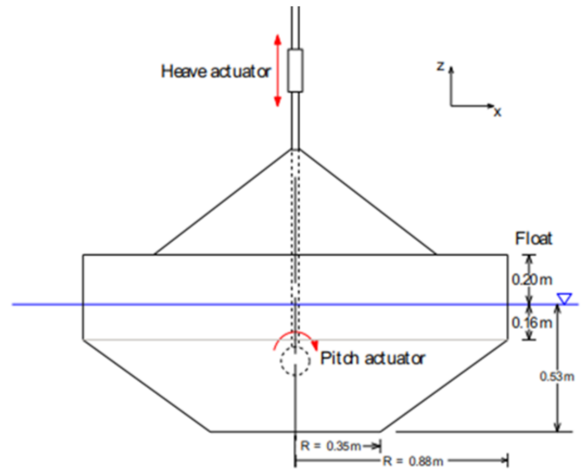

Figure 21 Geometry and dimensions of the heaving float

6.2.1 Hydrodynamic coefficients

Sandia computed the hydrodynamic coefficients via WAMIT. Some participants used their own potential flow solver, and the meshed geometry was made available on request (on the Share Point site). The hydrodynamic coefficients included the added mass, radiation damping and wave exciting forces (including both diffraction and linear Froude Krylov forces). Additionally, the hydrodynamic coefficients calculated by WAMIT were compared to those determined experimentally through radiation tests of the float and showed good agreement.

6.2.2 Specified test cases and results

Test Group ID	Test Case	Specified Parameters
SE	Static equilibrium	Float mass and geometry
DC	Heave decay test	Initial heave displacement and PTO damping
RA & DF	Radiation and diffraction tests	Actuator force signal/Wave train time series
RW	Regular Waves	Wave train and PTO force time series data

The heave decay tests of the float were purely numerical and there was no experimental data supporting the results. The results were like the sphere decay tests and showed good agreement between all simulations for the small release amplitude of 0.1meter. The results from the test are presented here are described in more detail in [19] .

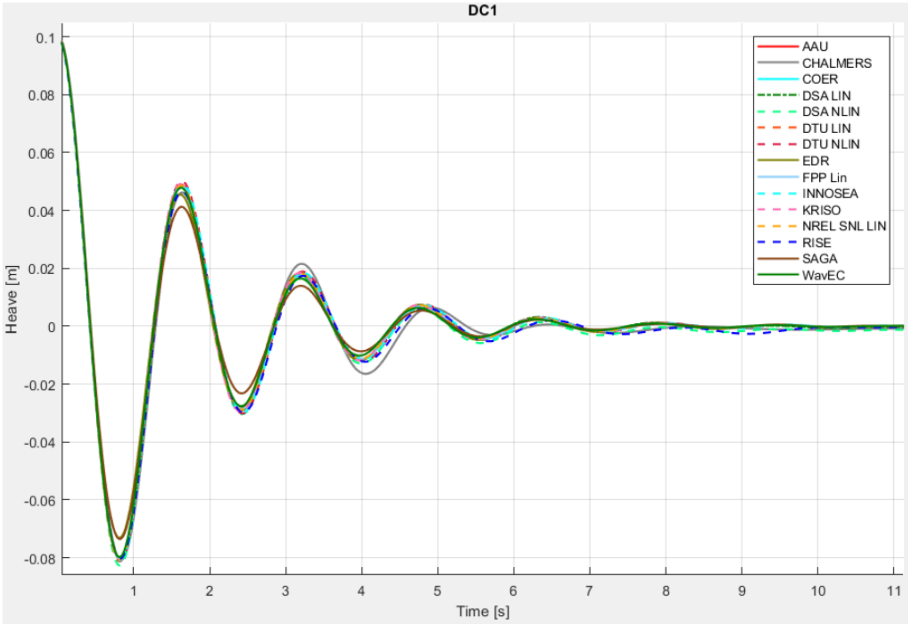

Figure 22 Calculated decay oscillation of the float from smallest drop height.

For the radiation tests, the float is forced to move in calm water. The goal of these forced oscillation tests is to compare the calculated response to the measured motion of the float for a given applied actuator force. The measured and calculated vertical float positions are compared as shown on the figure below. NREL provided force time series as input for the simulations.

Test ID	Actuator Frequency [Hz]	Estimated Motion Amplitude [m]
RA1	0.25	0.0665
RA2	0.6	0.1025
RA3	0.8	0.0668
RA4	1.0	0.0295

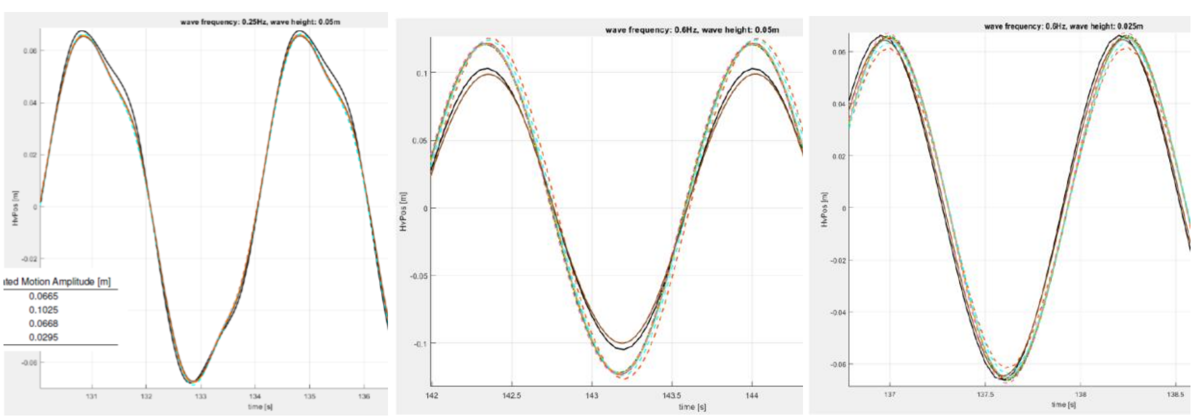

Figure 23 Measured float motion for given input force signal, radiation test RA1 4.0 sec, RA2 1.6 sec and RA3 1.25 sec.

The diffraction tests include the device locked in place and subjected to incoming waves. The vertical force measured on the device was used for comparison with the force calculated by the numerical models. The measured force signals for three of the four different diffraction tests are illustrated on Figure 24.

Test ID	Wave Frequency [Hz]	Wave Amplitude [m]	Steepness [m]
DF1	0.25	0.05	0.0006
DF2	0.6	0.05	0.0037
DF3	0.6	0.025	0.0018
DF4	0.9	0.05	0.0083

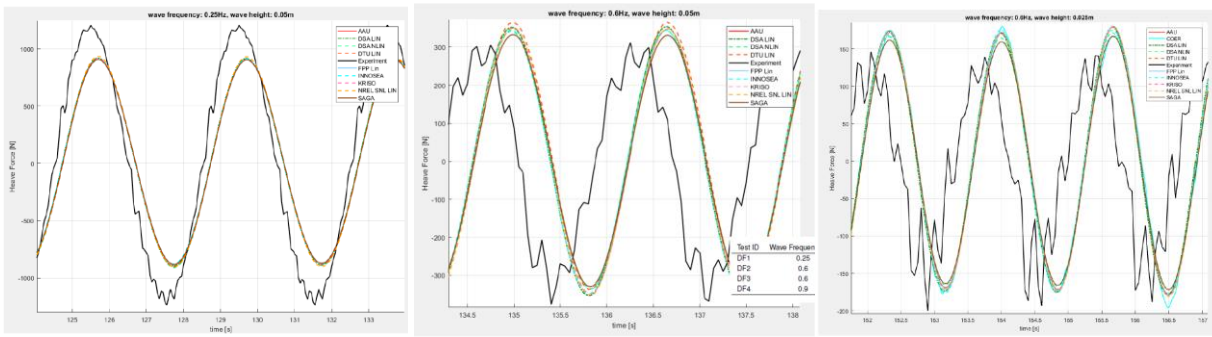

Figure 24 Measured and calculated vertical force on fixed float in incoming wave of DF1 4.0 sec, DF2 and DF3 1,6sec.

There was some uncertainty in wave elevation measurements, related to reflection and focusing effects in the basin and from the float. The best agreement was the most linear wave (DF1). The force measurement indicated fluctuations of higher harmonics, that could be caused by vibrations in the setup and/or nonlinear hydrodynamic effects.

Regular wave tests were simulated to calculate the response amplitude operator (RAOs) of the float and for the damped cases a stepped damping approach was used. To ensure that all participants simulate similar conditions, the PTO force time series, as well as the wave elevation time series was provided by NREL.

Test ID	Wave Frequency [Hz]	Wave Amplitude [m]	Steepness [m]
RW1	0.25	0.05	0.0006
RW2	0.30	0.05	0.0009
RW3	0.40	0.05	0.0016
RW4	0.50	0.05	0.0025
RW5	0.60	0.05	0.0037

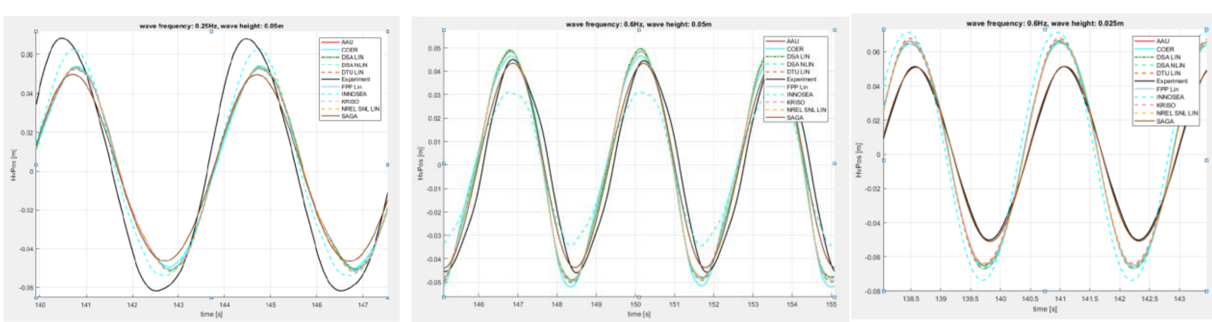

Figure 25 Results in regular waves of height 0.05m and period from left RW1 4 sec, RW2 3,3 sec RW3 2,5sec

Future dedicated test cases should include repetitions of experiments to provide confidence limits. Also experiments that could help understand the importance of non-linear hydrodynamics in the simulation of WECs would need to be developed.

6.3 THE KRISO OWC SYSTEM

Following the Mask basin test case, the OES group decided to find experimental data from an OWC type of WEC experiment. The objective of the new task was to gain experience in OWC code to experiment comparison using existing experimental data.

Korea Research Institute of Ships and Ocean Engineering (KRISO) had conducted experimental model test at scale 1:4 of a 30kW class OWC wave power plant in their 30 m by 56 m wave basin with a water depth of 3.2 m [28].

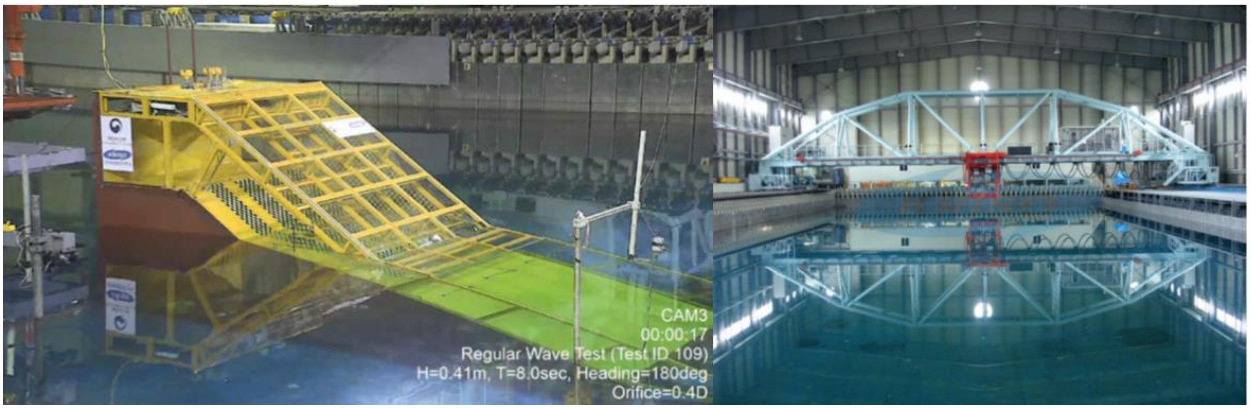

Figure 26 The Experimental test basin and model from the KRISO test

The KRISO data was supporting the development of a full-scale demonstration plant of the system in a breakwater at a Port on Jeju Island in Korea Figure 27shows the experimental model of the OWC structure with an inclined sloping chamber and duct for PTO. KRISO kindly offered the OES Task 10 group, to use these data for the next OES Task 10 simulation task.

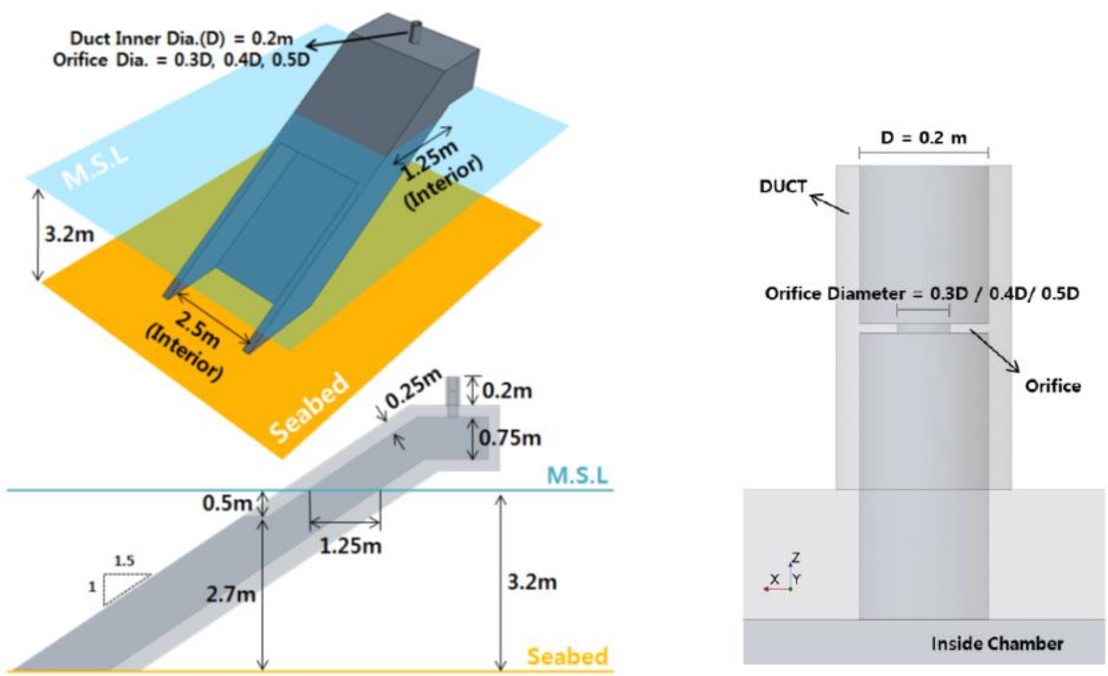

Figure 27 Geometry of the KRISO model

The test data included regular wave conditions with seven different wave periods ranging from T=2.25 s to 3.75 s and for each wave period three different wave heights ‘Low’ H ≈ 5cm,‘Med’ H ≈ 10 cm and ‘High’ H ≈ 20 cm. All waves fall in the linear wave regime with steepness less than 2 %.

Table 7 Monochromatic waves in model scale units

Period ID	T [sec]	H_{low}[m]	H_{med} [m]	H_{high} [m]
2	2,25	0,0450	0,0718	0,1794
3	2,5	0,0467	0,0925	0,2198
4	2,75	0,0459	0,0799	0,1918
5	3,0	0,0464	0,0845	0,1961
6	3,25	0,0454	0,0881	0,1959
7	3,5	0,0440	0,0890	0,2020
8	3,75	0,0480	0,0983	0,2090

Initially the reference waves were measured without the model in the basin at the location of the model, where the center of the OWC water surface would be located. The reference wave data was provided to all participants.

The air-turbine was simulated by an orifice placed in a duct of inner diameter D = 0.2 meter mounted on the upper part of the OWC. The air in the OWC chamber was pushed in and out through this duct. To produce different amount of damping on the OWC system the hole in the duct was partly blocked by an orifice of specified diameter. For all wave cases the orifice diameter of 0.4D was used and additional time series for diameters = 0.3D and 0.5 D was provided for the Medium high wave cases.

The test cases prepared for the group is shown on the Table 8 below, in total 35 time series.

Table 8 Test cases for the KRISO OWC experiments

Test Cases	**Variables**
Low Regular Waves	Wave period T, PTO setting (0,4D)
Medium Regular Waves	Wave period T, PTO setting (0,3D, 0,4D and 0,5D)
High Regular Waves	Wave period T, PTO setting (0,4D)

6.3.1 The measurments on the OWC

For OWC-type devices, special care needs to be taken to determine the pressure-flux relation for the flow through the orifice plate, or the model turbine, which is used to extract power from the system. Ideally, the pressure should be measured inside the OWC chamber and in the atmosphere at locations with smal air velocities to avoid local effects near the orifice/turbine. For each orifice a calibrated relation between the inhale and exhale flow and pressuredifference could in the ideal situation be established using a test bench. In the KRISO case the air velocity measurements were taken in two places one 3 cm below and one 3 cm above the center of the orifice. The pressure in the duct was measured three places above the orifice plate and three places below (12.5 cm from the plate) as shown in Figure 28. The pressure and flow velocity measurements were made available.

Also the water surface elevation inside the OWC chamber measured using 9 wave gauges mounted and aligned with the longitudinal direction of the chamber were made available.

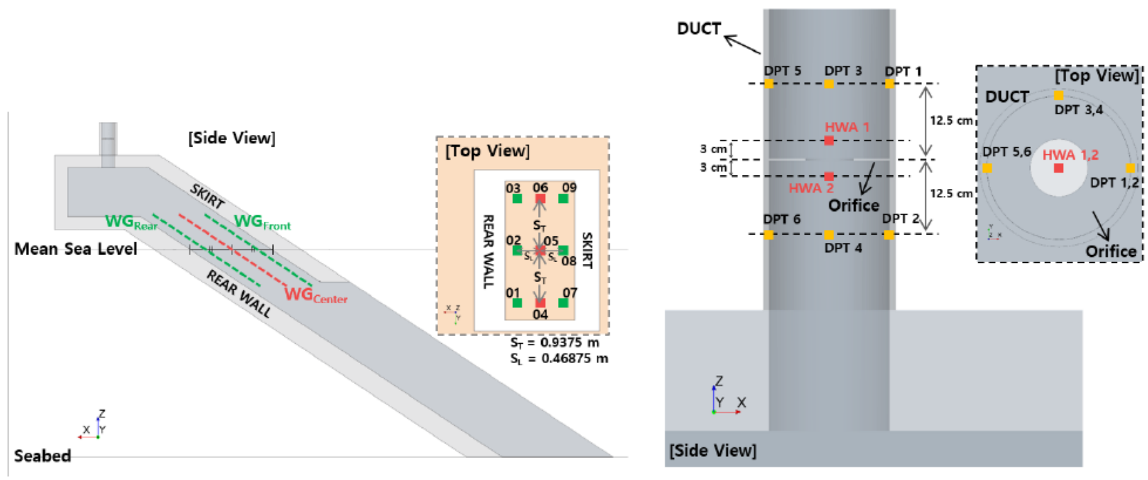

(**a**) Wave gauges. (**b**) Pressure and air flow gauges.

Figure 28 Location of measured date from the KRISO test

The measured surface elevation from 9 wave probes during test 106 with a wave height H=88 cm and the wave period T = 3.35s and the orifice 0.4D is shown on the plot below, as well as the measured pressure difference between the three set of pressure gauges below and above the orifice.

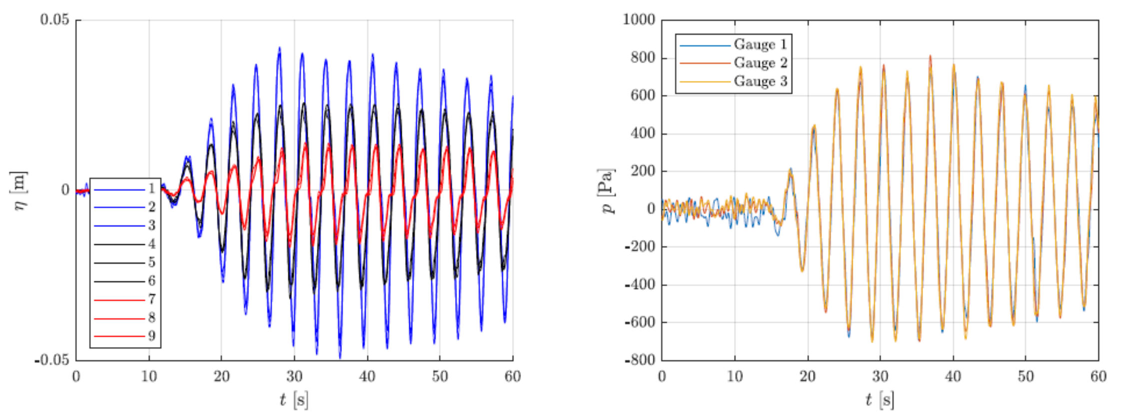

(**a**) Measured vertical chamber motions at the nine (**b**) Measured pressure difference across the orifice

Figure 29 Measured surface elevation at the 9 wave gauges (a) and pressure difference (b) between the three set of pressure gauges for Test 106

In the KRISO test case there was some uncertainty related to the exact value of the discharge coefficient c_d and two values were used to investigate the difference 0.64 and 0.8271. Discharge coefficient c_d can be determined based on calibration tests, between measured flow and pressuredrop over the orifice. The resulting flow based on cd = 0.82 is shown in the plot below compared to flow calculated from the measured velocity at the orifice u_a and based on the measured velocity of the water surface elevation in the chamber $\bar{\eta}$

1. $Q = A_c \bar{u}$, $where\ \bar{u} = \partial_t \bar{\eta}$ with $\bar{\eta}$ the mean of the nine internal wave guage measurements and ∂_t the time derivative and A_c the surface area of the water column.
2. $Q = A_0 u_a$, $where\ \ u_a$ is the measured air flow velocity through the orifice opening area A_0 [m^2]. Here, it was determined that the most accurate result was found by taking the measured velocity value from the upper gauge for the outflow and from the lower gauge for the inflow.
3. $Q = C_d A_0 \sqrt{\frac{2}{\rho_a} |\bar{p}|}\ sign\ (\bar{p})$, where ρ_a is the density of air (1,2 kg/m3 and $\bar{p}$ is the mean pressure difference of the three measurements

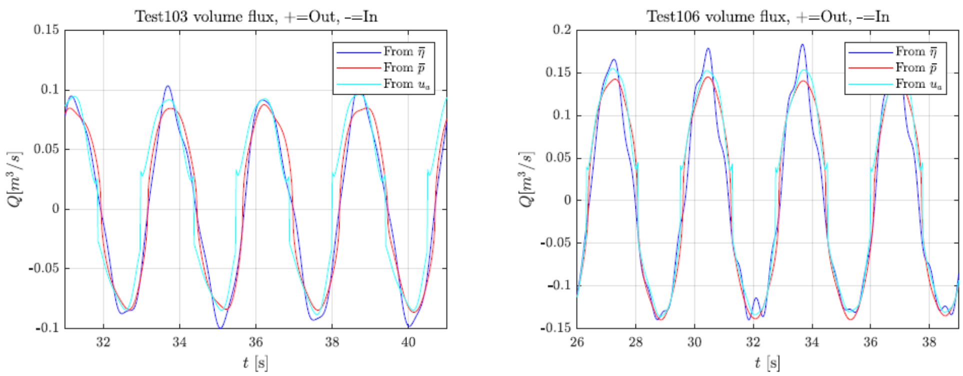

Figure 30 Volume flux calculated using the 3 methods above for Test 103 and Test 106

The power absorbed P_{abs} [watt] by the OWC from the waves are calculated as the product of flow Q and pressure difference $\bar{p}$.

$$P_{abs} = \bar{p} Q$$

$\bar{p}$	[Pa]	Pressure difference (P-P_0) over the orifice relative to atmosphere (1 mm H_2O = 10 Pa)
Q	[m^3/s]	Flow of air

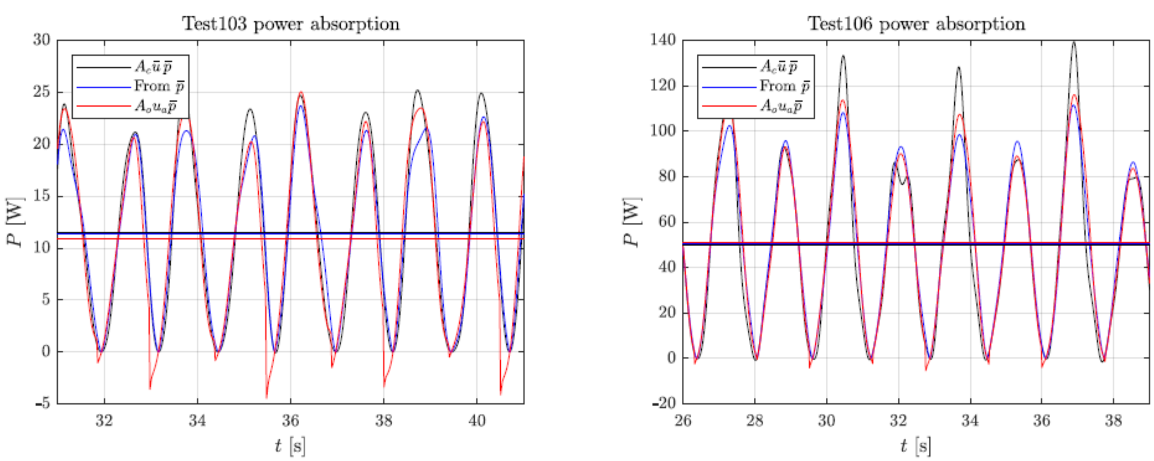

Figure 31 Power absorption calculated using the 3 methods above for Test 103 and Test 106

The data calculated by the teams was specified as in the table below.

Table 9 Output format description for OWC test

Column	Description
1	Time [sec]
2	Wave elevation at the chamber center [m] (no chamber in the tank)
3	Wave elevation inside the chamber [m] (location 2)
4	Wave elevation inside chamber [m] (location 5)
5	Wave elevation inside chamber [m] (location 8)
6	Wave elevation inside chamber [m] (average)
7	Pressure difference across the duct [Pa]
8	Volume flow [m3/s]
9	Absorbed hydrodynamic power [W]

The numerical models that have been applied in this study to predict the KRISO OWC chamber response and power absorption included: weakly-nonlinear potential flow theory in the frequency domain, weakly-nonlinear potential flow theory in the time domain, and CFD. Both compressible- and incompressible-flow models are applied to the air phase. These models are described in [20]. The results of the calculated surface elevation in the center of the chamber as a function of time are shown below Figure 32 for the CFD_I incompressible and CFD_c compressible modles, Time Domain TD_I incompressible and TD_c compressible for Cd=0.82 and Cd =.65 repectively and the KRISO Experimental. It should be noted that there is an excellent agreement between the CFD_c model and the experiments.

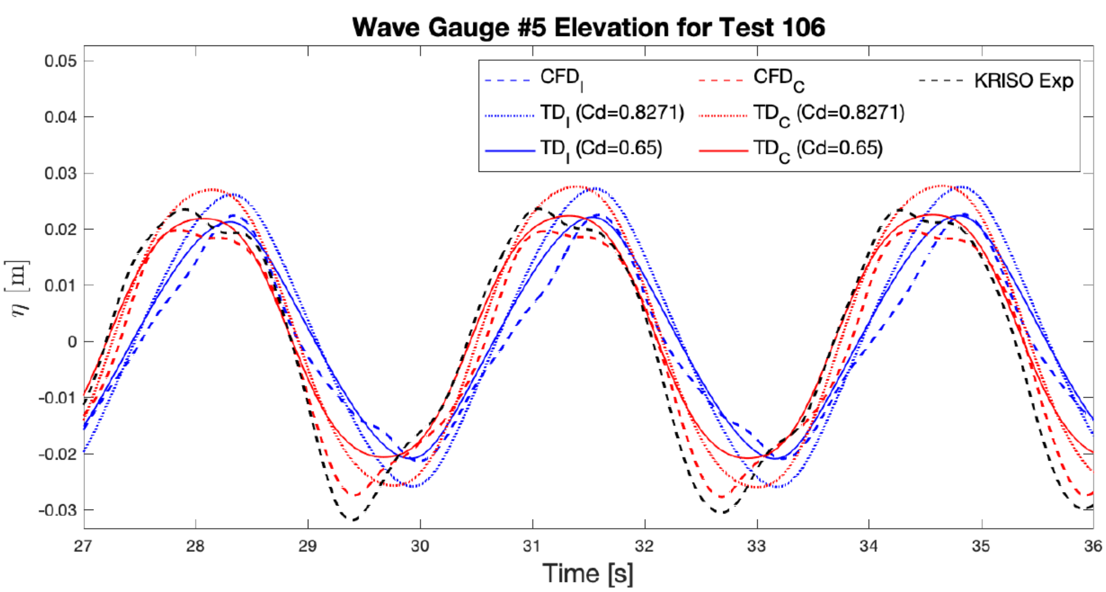

Figure 32 Surface elevation in the center of the chamber from KRISO OWC experiment, measured and calculated using CFD simulations and potential flow solutions (test 106)

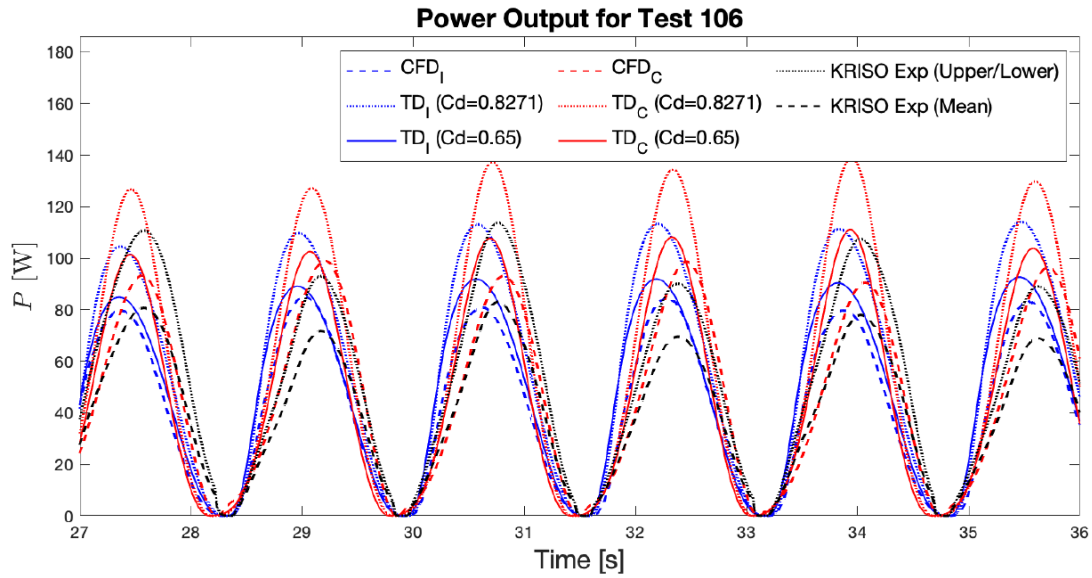

Figure 33 Estimated power output from KRISO OWC experiment, CFD simulations and potential flow solutions (test 106)

A short summery of quotes from the paper [19]: *"A set of relatively large-scale measurements for a breakwater-mounted OWC chamber has been carefully analyzed and compared with numerical predictions based on weakly-nonlinear time – and frequency-domain potential flow methods, and CFD. The air-phase has been modeled using both incompressible- and compressible-flow models."*

"For weakly-nonlinear potential flow models, the interior chamber response is typically assumed to be a superposition of standing-wave modes. The hydrodynamic characteristics of these modes can be treated either through the introduction of so-called free-surface pressure (FSP) modes, as was done for example by Bingham et al. [21], or by treating the surface as a massless flexible plate and introducing generalized modes for the response of this plate [1]. Both methods require distributing panels directly on the free surface, which leads to singular matrices in the limit as the frequency ω goes towards infinity. One of the contributions of H Bingham DTU to this task is to illustrate a simple method for accurately computing the added mass, which is critical for time-domain modelling."

"For CFD methods, the main issues are associated with properly resolving the two-phase fluid interaction between the water and air inside the chamber, if the air phase is compressible. The effects of air compressibility are found to be small for the pressure difference across the orifice plate, but they produce significant nonlinear effects and a significant phase-shift of the internal chamber surface motion. All models capture the time-averaged quantities well, but only the compressible CFD model can accurately reproduce the detailed responses."

"This task revealed several important guidelines to produce benchmark experimental data suitable for comparing the relative accuracy of different levels of numerical modelling. Ideally, benchmark data should include repetition of each case, so that

the uncertainty of all measured quantities can be quantified to produce reliable confidence bounds. This begins with the undisturbed wave conditions in the basin without the structure in place. Then, all measured quantities with the structure in place. Once the realization uncertainties are established, they can be combined with measurement errors to establish 95% confidence intervals, which then allow the data to be used to precisely evaluate the accuracy of the numerical models."

"For OWC-type devices, special care needs to be taken to determine the pressure-flux relation for the flow through the orifice plate, or the model turbine, which is used to extract power from the system. Ideally, the pressure difference should be measured between the chamber and the atmosphere to avoid local effects near the orifice/turbine."

Since the study was completed by the OES Task 10 on the KRISO experimental data – KRISO has built and installed the WEC. Sea trial operation started in October 2021 of the grid-connected full-scale sloped Oscillating Water Column power plant, including an impulse air turbine, permanent magnet synchronous generator, AC-DC converter, energy storage system and integrated control system. Results from the first year of testing can be found in [23].

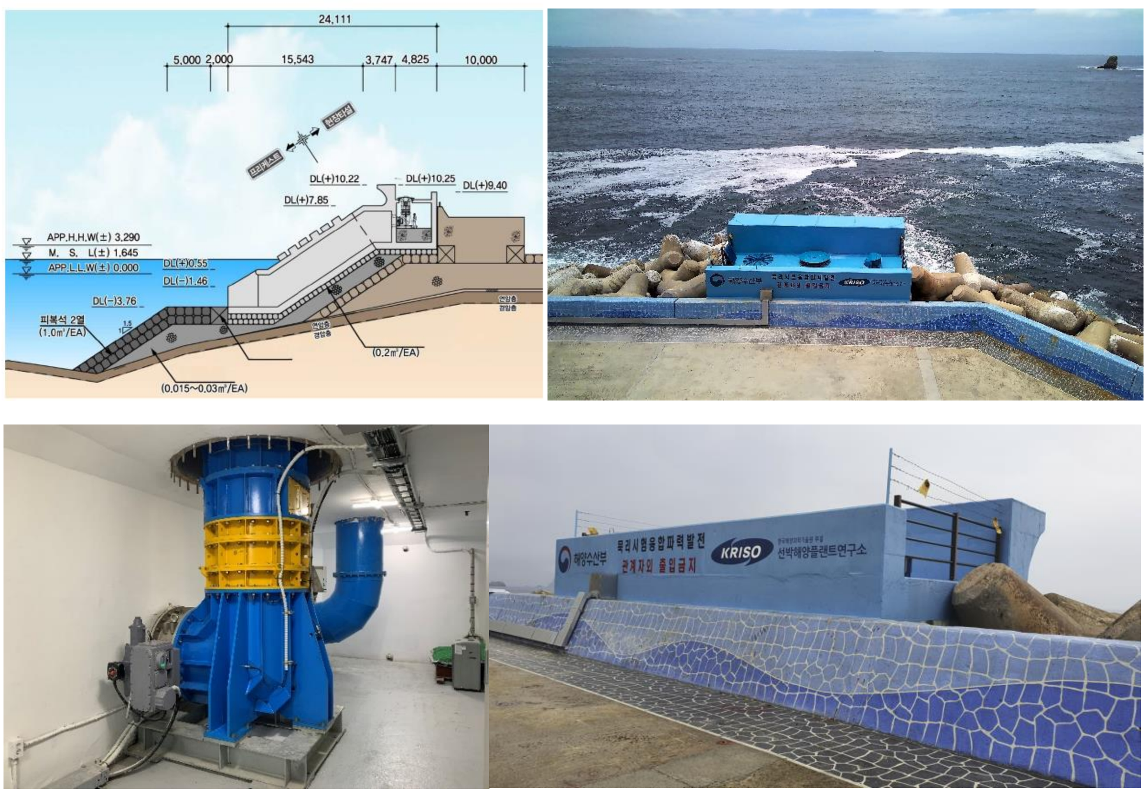

Figure 34 full-scale sloped Oscillating Water Column power plant Port on Jeju island Korea

6.4 THE DTU OWC TEST CASE

As the fourth test case DTU kindly proposed using their existing data from tests with a fixed OWC chamber at scale 1:50 mounted on the side of a DTU wave flume. The experimental setup resembles an array of double chamber OWCs, where the wall with the chamber attached acts as the centerline, and the opposite flume wall acts like a mirror. The distance between the chambers is then (120 cm) twice the flume width, as shown Figure 35. The double chamber represents a section of KNSwing a floating attenuator with multiple OWC chambers open to each side of its hull [24].

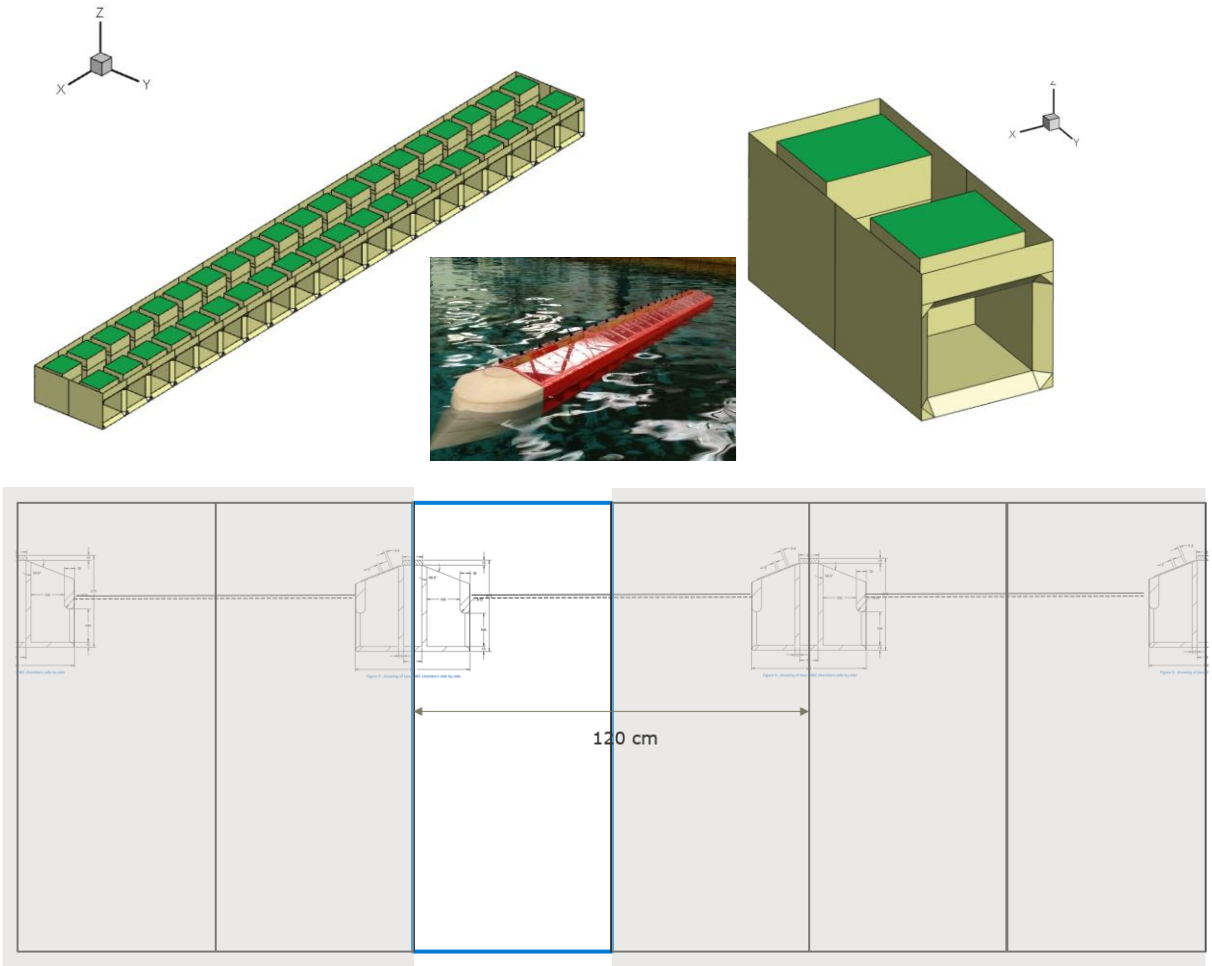

Figure 35 OWC scale chamber model and mirror effect

The OES Task 10 group participating in the DTU OWC task consisted of DTU, AAU, NREL and Ramboll, and SSPA, University of the Faroe Islands, Maynooth University, Saga University, MARIN, National University Taiwan. SSPA Maritime Center.

6.4.1 The Experimental model

The geometry of the DTU fixed OWC chamber is shown Figure 36 including a photo of the model mounted on the side of the wave flume. The two internal chamber wave probes WG7 and WG4 are placed 10mm from the back and front walls of the chamber.

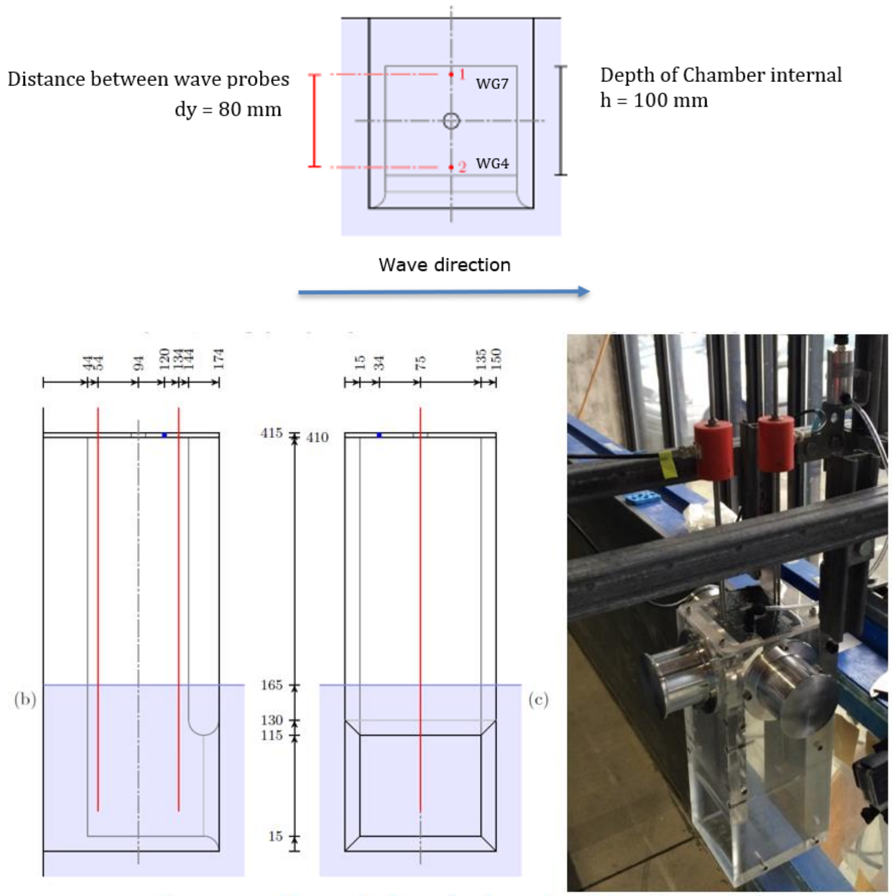

Figure 36 the geometry of the DTU fixed OWC chamber scale model, top, front, and side view

The main dimensions of the blue shaded submerged part of the model chamber are shown in Table 10 – as well as in full scale.

Table 10 General properties for the OWC full scale and in scale 1:50

Parameters	Model Value	Full scale
Chamber length	120 mm	6 m
Chamber depth	100 mm	5 m
Opening height	100 mm	5 m
Depth of lip	50 mm	2.5 m
Thickness of lip	30 mm	1.5 m
Thickness of side walls	15 mm	0.75 m
Orifice diameter	16 mm	0.8 m
Water depth	650 mm	32.5 m
Water density ρ_w	1000.0 kg/m^3	1000.0 kg/m^3
Air density ρ_a	1.2 kg/m^3	1.2 kg/m^3

The DTU wave flume is 23.5 m long 0.6 m wide and the water depth 0.65 m as shown in Figure 37. The OWC chamber is mounted on one side wall of the flume, in the central part. The wave maker is located at one end of the flume and at the other end there is an absorbing beach. In the experiment, 5 wave gauges are placed at the shown locations to measure the waves, and 2 are mounted inside the chamber to measure the surface motion in the OWC. In addition, there is a pressure sensor mounted in the roof of the OWC to measure the pressure inside of the chamber relative to the external atmosphere pressure.

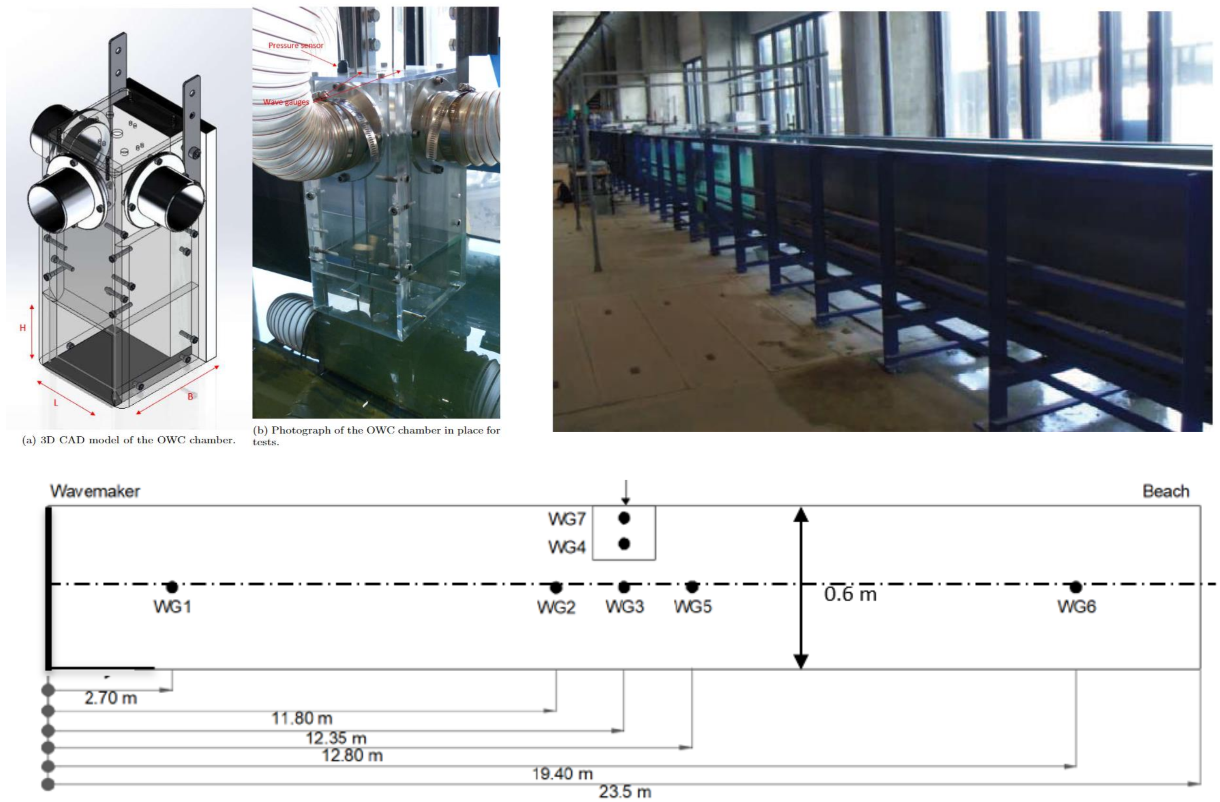

(a) 3D CAD model of the OWC chamber.

(b) Photograph of the OWC chamber in place for tests.

Figure 37 Illustration of the experimental setup of the fixed model of the OWC in the 60 cm wide wave flume

The linear hydrodynamic coefficients for the model are computed using the still-water submerged geometry of the chamber. These coefficients include the added-mass, radiation damping and wave exciting forces. DTU provided the geometry file and linear coefficients for the OWC chamber using WAMIT [3], and NREL uploaded these data to the NREL SharePoint, made available to the group.

6.4.2 Case Specifications

The experimental regular wave cases included 15 wave periods from 0.57 sec to 1.64 sec and for each period two wave heights of steepness's 2.5% and 4 % as shown in Table 11 below. The data was initially measured without the model in the flume, then followed by data measured with model in the flume. The wave elevation at two points WG 4 and WG7 inside the chamber for the un-damped case was provided. The chosen wave heights are almost linear in theory. Also, the measured pressure inside the chamber was provided for the damped cases after the teams had uploaded their calculations as a blind study.

Table 11 Specification of Cases considered.

T	λ	T/T_0	H_1	H_2	tmax	tstop
			H/λ =0.025	H/λ =0.040		
sec	m	-	m	m	sec	sec
0.57	0.51	0.70	0.013	0.021	84	140
0.74	0.85	0.90	0.021	0.034	65	109
0.78	0.94	0.95	0.024	0.038	62	103
0.79	0.98	0.97	0.025	0.039	60	100
0.81	1.02	0.99	0.026	0.041	59	98
0.82	1.05	1.00	0.026	0.042	58	97
0.83	1.07	1.01	0.027	0.043	58	96
0.84	1.11	1.03	0.028	0.044	57	94
0.86	1.15	1.05	0.029	0.046	55	92
0.90	1.26	1.10	0.032	0.050	52	87
0.98	1.49	1.20	0.037	0.060	47	79
1.15	1.98	1.40	0.050	0.079	38	64
1.31	2.48	1.60	0.062	0.099	32	53
1.47	2.98	1.80	0.074	0.119	27	46
1.64	3.46	2.00	0.087	0.138	24	41

Based on the experimental measurements, and the assumption of an incompressible flow through the orifice plate, the pressure-flux relation is well-described by:

$$Q = C_d A_0 \sqrt{\frac{2}{\rho_a}|\bar{p}|}\, sign\,(\bar{p}),$$

$$Q = A_c \bar{u}\,, where\ \bar{u} = \partial_t \bar{\eta}$$

with $\bar{\eta}$ the mean of the two internal wave guage measurements and ∂_t the time derivative and A_c the surface area of the water coullmn.

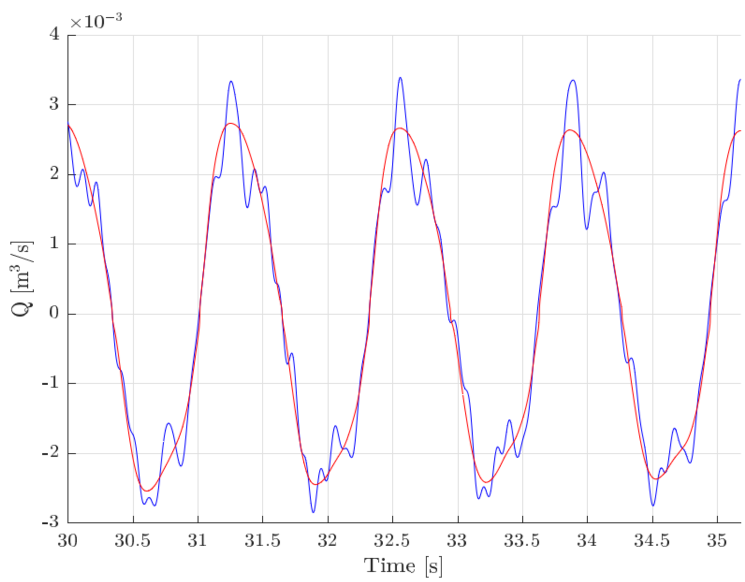

Figure 38 Comparison of the air-volume flux computed from the pressure measurement Eq. 1 (red curve) and the air-volume flux computed from the 2 wave probes Eq. 3 (blue curve). H=0.099m T=1.31s. Cd=0.64.

The RAO of the OWC column depends on the applied damping of the airflow in and out of the chamber. Four different PTO conditions will be considered:

1. Open chamber – no PTO damping (see figure 1)
2. Fixed orifice case (Ø16mm)
3. One-way damping – venting on the upstroke (see geometry Appendix 1)
4. One-way damping – venting on the down stroke (see geometry Appendix 1)

The participating partners were asked to provide time series of the following parameters, for the comparison with the experimental results and with each other.

Column	Description
1.	Time [s]
2.	Wave elevation at WG 3, without the chamber [m]
3.	Surface elevation at WG 4 (inside the chamber) [m]
4.	Surface elevation at WG 7 (inside the chamber) [m]
5.	Pressure in the Chamber [N/m^2]
6.	Flow through orifice [m^3/s]
8.	Absorbed power [W]

The results of experiments carried out in regular waves of two steepness values, were compared to computed responses for both two-way and one-way energy absorption strategies.

6.4.3 Two-way damping

The two-way absorption is the case where the air in the OWC camber is pushed out and sucked in through the fixed orifice. This is called two-way damping of the water column, as the water column is damped on both the upstroke and the down stroke.

> The paper [27] concludes: *"This seemingly simple test case clearly holds many challenges both for numerical analysis and for experimental measurement. In the first round of comparisons, the spread was dramatic which allowed the teams to identify minor bugs and inconsistencies in their calculations and arrive at the final consensus. This is a good lesson that even seemingly simple cases can be prone to simple errors, highlighting the benefit of comparing independent calculations of the same case.*
>
> *For two-way absorption, measured and computed pressures and CWR generally agree quite well. Although we have not carefully estimated a confidence bound for the experimental uncertainties in these measurements, the calculations are mostly within what we expect those bounds to be. The exception is the MARIN results which are substantially lower than the others, presumably because the viscous damping has been over-estimated in this model."*

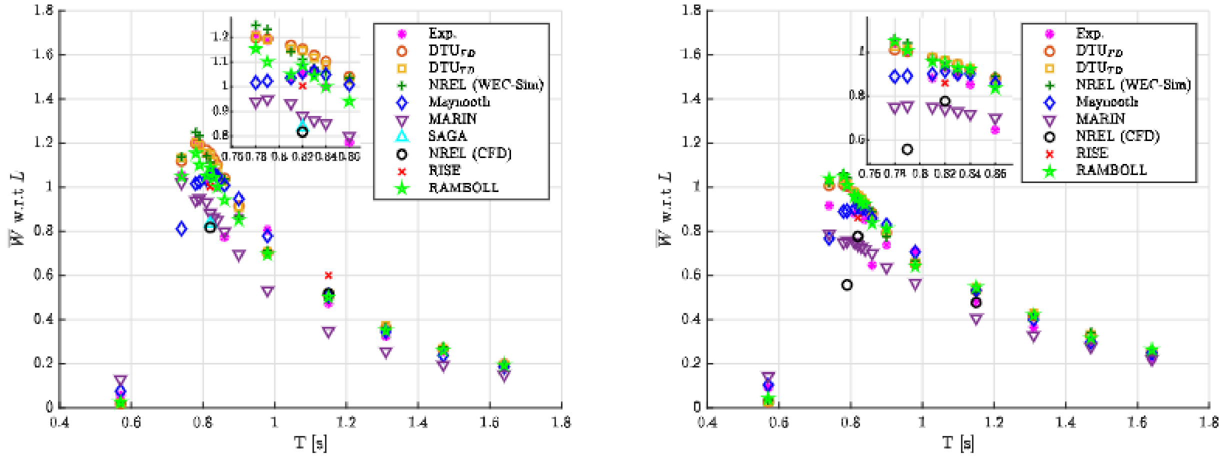

(a) $H/\lambda = 0.025$. (b) $H/\lambda = 0.04$.

Figure 39 Capture-width-ratio, two-way absorption

The CFD models agree well with each other and with the experiments at T = 0.82s for both wave steepness values. At the lower steepness with at T = 1.15s, the NREL-CFD and experimental results are very close, but the RISE results are somewhat lower. For the higher steepness value in Fig. 14b, the NREL-CFD point at T = 1.15s also agrees well with the experiments, while the RISE result is somewhat lower. The NREL-CFD value at T = 0.79s is substantially lower than the experiments.

A representative period of the absorbed power time series for T = 0.82s is shown in Figs. 15a and 15b. The figures show similar trends as for the pressure.

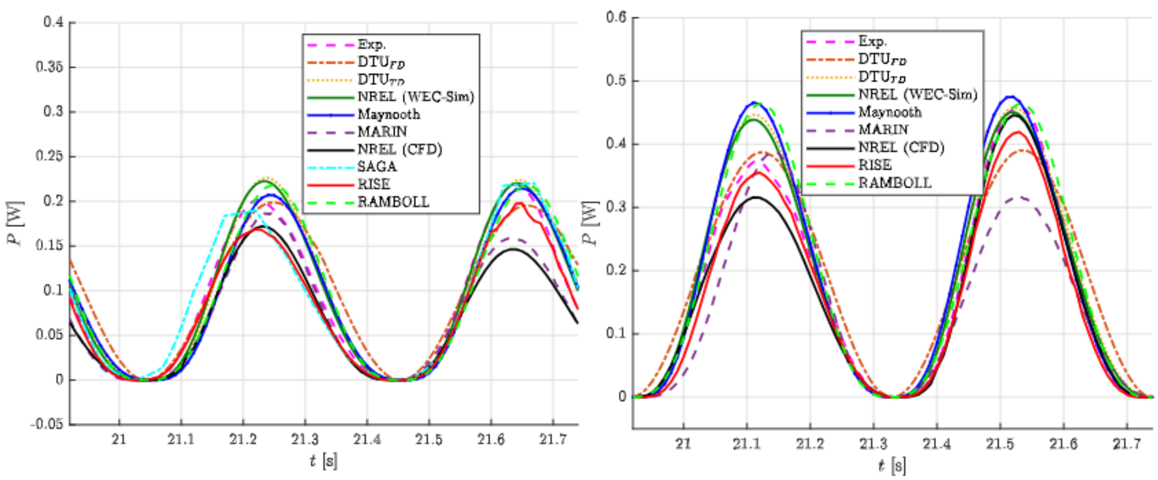

(a) $H/\lambda = 0.025$. (b) $H/\lambda = 0.04$.

Fig. 15: Absorbed power at $T = 0.82$s, two way absorption.

For one-way absorption however, we find a much larger spread in the numerical predictions which generally predict a much larger energy absorption than the measurements. It is clear from the measurements that the passive one-way valve system used for these experiments allowed for significant energy loss on the passive cycle, which we contend explains a large part of the discrepancy, though this must be confirmed by new measurements using a better release valve system. The MARIN results here are generally close to the experiments, indicating that the choice of viscous damping captures a similar overall energy loss. The two CFD results at the natural period also agrees well with the experiments, but it is worth mentioning that modelling the release valve in these calculations was also challenging and some energy loss on the passive cycle is also clear in the associated time-series of pressure. The rest of the potential flow calculations agree relatively well with each other, though the influence of the channel walls is more pronounced here than it was in the one-way case.

(a) (b)

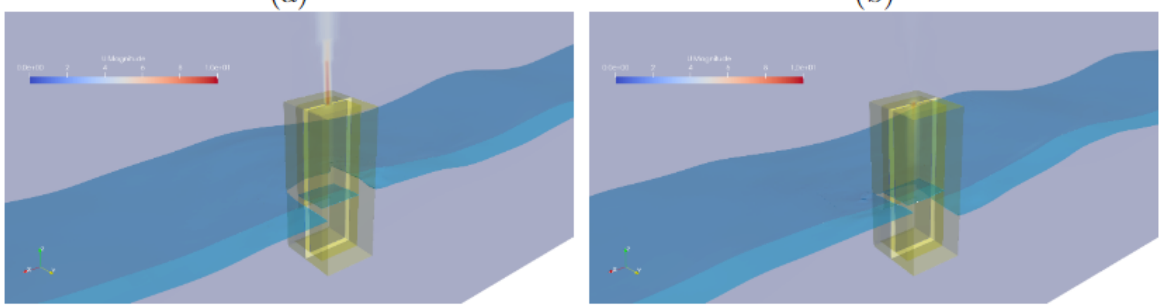

Fig. 10: Snapshots of the (a) exhale and (b) inhale of the two-way absorption simulations of RISE ($T = 0.82$s and $H/\lambda = 0.025$).

The results highlight the challenges associated with this seemingly simple device, especially with the one-way absorption strategy which is difficult to perfectly implement both physically and numerically. Potential flow calculations predict that as much, or in some cases more, energy can be absorbed using the one-way strategy, but the opposite is shown by the measurements and CFD calculations. However, a better physical release valve system is required to confirm this one way or the other. A better release valve model in the CFD calculations should also be developed and more calculations performed to illuminate the physics of the one-way response.

7 CONCLUSIONS

The collaboration under OES Task 10 has provided a platform where different model teams can interact and compare their numerical results from simulating the same WEC systems using their own numerical models. Good agreement between the results presented gives confidence, as for example, if the power output from a specific WEC calculated by different team members shows the same result. This confidence is valuable for stakeholders that want to evaluate the performance of a WEC during the first stages of development.

The collaboration also showed that even experts working on seemingly simple cases can make simple errors, highlighting the benefit of having time to compare independent calculations of the same case.

The development of wave energy converters (WECs) today relies to a considerable extent on numerical simulations to optimise and evaluate their designs and to provide the power performance estimates that feed into the levelized cost of energy (LCoE). The “performance before readiness” path, put forward by Weber [1] argues that it is most economical to make the optimization and major design choices early in the development process, to achieve a high Technology Performance Level (TPL), which indicates a low LCoE, before building and deploying a costly WEC at a higher Technology Readiness Level (TRL). The “performance before readiness” path requires iterations of optimizations using numerical tools and validations of components using physical tests, and thus the confidence in the use of numerical tools must be unquestioned.

International networks and collaboration under Task 10 is also welcoming for early-stage researchers entering the fields of Ocean Energy. This is to emphasize the importance of a critical approach to numerical modelling results and in this respect to use an analytical mindset.

The permanent status of the OES task 10 is there also to encouraging researchers to be critical on evaluating their numerical results and ensure they look at lesson learned through modelling and use this knowledge when evaluating potential project applications.

The validation of numerical simulation methodologies leads to

a. Reduced risk in technology development
b. Improved WEC energy capture estimates (IEC TC 102, ...
c. Improved load estimates
d. Reduced uncertainty in LCOE models

Such validation therefor helps establish confidence in the results provided by numerical WEC models and WEC modelers.

8 FUTURE WORK

In this chapter we will go through the initial scope and objective as formulated in seven subtasks and see how far we are and what would be the logical next steps.

8.1 SURVIVAL CONDITIONS & DESIGN LOADS

Extreme waves impose the larges forces and motions on the WEC, and we need to validate the numerical tools and methods used today for WEC design and examine the loads and safety limits.

Here we can define the 50- and 100-year return periods associated with the measured wave data from a particular site. A design basis, including all assumptions, environmental conditions, etc. Refer to IEC/TS 62600-2: Marine energy – Wave, tidal and other water current converters – Part 2: Design requirements for marine energy systems. Edition 1.0, 2016-08.

A significant wave height with a 100-year return-period is on the order of 10 – 13 meter high with a peak wave period of about 17 seconds for a typical site with an average resource of about 20 – 30 kW/meter. These values can be used to determine the design loads on the structure.

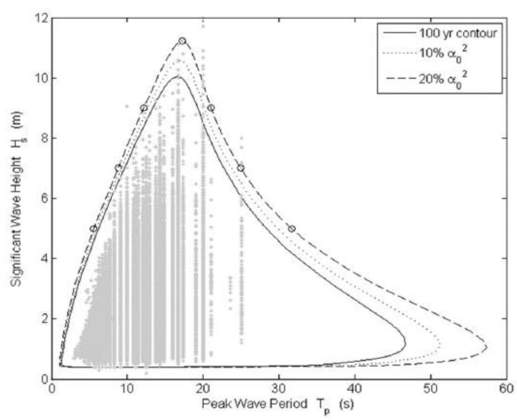

Figure 1-4: 100-year contour for NDBC buoy 46022 (Berg 2011).

Figure 40 Example of 100 year countor of significant wave height as a function of Peak Wave Period

8.2 ADDITIONAL EXPERIMENTAL TEST DATA

Discuss the need, practicality, and cost of obtaining additional experimental test data for model validation and making written recommendations to the ExCo and the technical community. Recommendations will consider the following component measurements:

- Structural loads
- Survival modes of the PTO
- Survival modes of the mooring system
- New WEC test data for validation
- Innovative concepts
- Device archetypes that are lacking in experimental data

9 ANNEX WITH EXAMPLE CALCULATIONS

The simulation of the heaving sphere involves a description of the geometry and wave conditions.

9.1 HEAVING SPHERE GEOMETRY

The floating sphere investigated is restrained to heave motion only. It has a radius of a=5.0 m, and its origin is located on the mean water surface, at the center of the spherical body. The center of gravity is located 2.0 m below the mean water surface. A summary of the most important model parameters is shown on Figure 41. The initial test specified for the group of IEA OES Task 10 participants was the calculate the hydrostatic loads, determine the hydrodynamic coefficients compared with theory and calculate heave decay test of the sphere in still water.

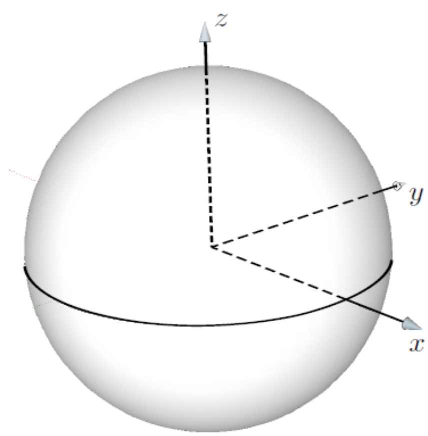

Parameter	Value
Mass	261.8×10^3 kg
Centre of Gravity	(0, 0, -2) m
Radius	5 m
Draft	5 m
Water Depth	infinite
Water Density	1000 kg/m^3

Figure 41 Sketch of the heaving sphere and general properties

9.1.1 Hydrostatic

The hydrostatic test is without any waves, just flat water – one test is to ensure that the float floats at the prescribed waterline, in this case specified on equator. The float mass M_f must equal the mass of the volume of displaced water, which for a half sphere with radius a is:

$$M_f = \rho \frac{2}{3} \pi a^3$$

On the Figure 42 below you see how the hydrostatic force varies as a function of the displacement of the float ξ_3 and the hydrodynamic stiffness C_{33} = Aw*ρ*g, where $A_w = \pi a^2$ is the water plain area at equator

$$Fbnl(\xi_3) = C_{33}\xi_3 \left(1 - \frac{{\xi_3}^2}{3 \cdot a^2}\right)$$

Linear theory is approximations where all excursions are assumed very small – and as example the hydrostatic force would vary proportionally with the displacement ξ_3 and the water surface area A_w as showed with green line on Figure 42.

$$Fhs(\xi_3) = C_{33}\xi_3$$

This linear variation of force agrees well with the actual displaced volume for small excursions with amplitudes (smaller than in this case 1,5 meter). The nonlinear buoyancy force reaches a maximum or minimum constant value when the sphere is either fully submerged or completely out of the water. The linear force calculation is at these excursions 1.5 times higher compared to the actual load.

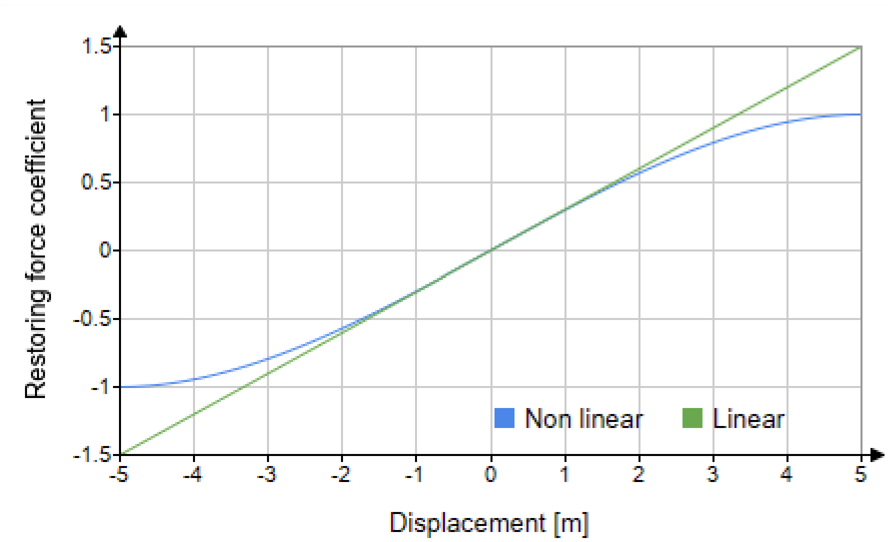

Figure 42 Hydrostatic force on the floating sphere

9.1.2 Hydrodynamic parameters

The sphere was chosen as example, because it is possible to derive an analytical solution to the frequency-dependent hydrodynamic properties such as added mass and damping. Such a solution and results were first presented by Havelock (1955) [29] and Hulme (1982) [30]. A comparison of the early analytical values to calculations of values carried out using the modern computer program, WAMIT Lee & Newman (2015) is shown in Figure 43. To compare WAMIT values with the theoretical values derived by Hulme (1982), the WAMIT coefficients have been nondimensionalized accordingly.

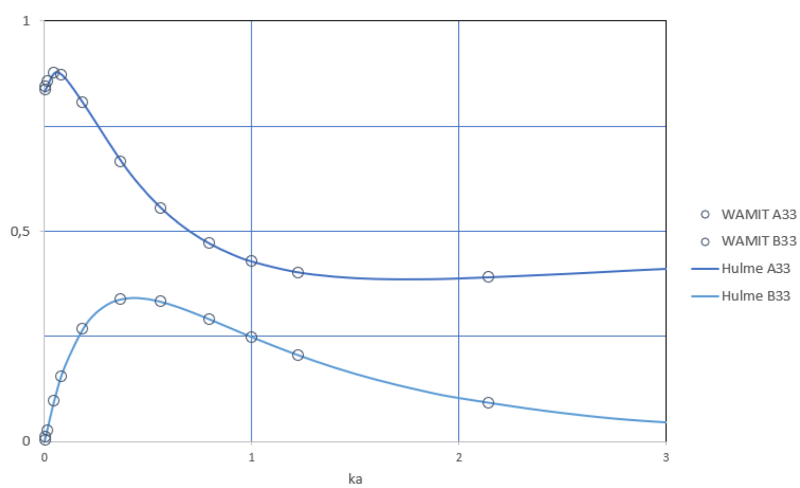

Figure 43 Comparison of analytical coefficients (Hulme, 1982) and coefficients derived using WAMIT.

Researchers at the National Renewable Energy Laboratory (NREL) generated the coefficients to be used by all IEA OES Task 10 participants. Table 12 shows examples of selected values of the calculated coefficients using WAMIT computed at the center of gravity (CG) and at the mean water surface. The hydrodynamic coefficients include the added mass, radiation damping and wave-exciting forces, including both diffraction and linear Froude–Krylov forces.

Table 12 The hydrodynamic coefficients B33 and A33 for selected values of T in deep water.

T	λ	ka	B33 (T)	B'33 (T)	A33 (T)	A'33(T)	X3(T)	X'3(t)
Sec	m	-	kg sec-1		Kg			
3.0	14.1	2.23	4.70×10^4	0.086	1.03×10^5	0.39	9780	0.127
4.0	25.0	1.25	8.24×10^4	0.200	1.05×10^5	0.40	20030	0.260
4.4	30.2	1.04	8.98×10^4	0.240	1.11×10^5	0.42	29960	0.389
5.0	39.0	0.805	9.46×10^4	0.288	1.22×10^5	0.47	38700	0.502
6.0	56.2	0.559	9.17×10^4	0.334	1.45×10^5	0.55	45750	0.594
7.0	76.5	0.411	8.06×10^4	0.343	1.67×10^5	0.64	51430	0.668
8.0	99.9	0.315	6.87×10^4	0.334	1.84×10^5	0.70	55740	0.724
9.0	126.4	0.248	5.68×10^4	0.311	1.97×10^5	0.75	59230	0.769
10.0	156.1	0.201	4.65×10^4	0.283	2.07×10^5	0.79	62350	0.809
11.0	188.9	0.166	3.89×10^4	0.260	2.16×10^5	0.83	64730	0.840

The deepwater wavelength is.

$$\lambda = \frac{g}{2\pi}T^2$$

And the dimensionless variable ka is defined as

$$ka = 2\pi\frac{a}{\lambda} = \frac{4\pi^2 a}{gT^2}$$

B'33 is nondimensionalized with weight displaced volume times ω of the float $\frac{2}{3}\pi a^3\rho\omega$

A'33 is nondimensionalized with weight of displaced water by the float $\frac{2}{3}\pi a^3\rho$

X'3 is nondimensionalized with hydrostatic stiffness coefficient C_{33}

Where

$$\omega = \frac{2\pi}{T}$$

The general equation of forced motion of the asymmetric body in heave is reduced using j=3 and k=3 in the equation below:

$$\sum_{k=1}^{Nd}\left[-\omega^2(M_{jk} + A_{jk}) + \mathrm{i}\omega\left(B_{jk} + B_{jk}^0\right) + (C_{jk} + c_{jk})\right]\xi_k = X_j \qquad where\ \ j = 1,2,\ldots\ldots N_d$$

9.1.3 Decay test

The second task was to simulate how the float moves up and down if there are initially no waves in the water and the sphere is released from a given initial elevation x_0. The similarity with the damped oscillator is explained as the spring term comparable to the hydrostatic stiffness C_{33} = Aw*ρ*g and the damping force proportional to the hydrodynamic damping coefficient $B_{33}(T)$ and the inertial part proportional with the acceleration is expressed as the sum of the float mass M_f plus added mass $A_{33}(T)$.

$$(M_f + A_{33}(\omega))\ddot{\xi_3} + B_{33}(\omega)\dot{\xi_3} + C_{33}\xi_3 = 0 \qquad (2)$$

The natural cyclic frequency of the oscillation if there was no damping would be ω_0 defined as:

$$\omega_0 = \sqrt{\frac{C_{33}}{M_f + A_{33}(\omega_0)}}$$

The theoretical solution for equation is found using.

$$\xi_3(t) = (C_1 cos\omega_d t + C_2 sin\omega_d t)e^{-\delta(\omega_d)t}$$

The constants C1 initial position x_0 C2 depends in addition on the initial velocity u_0 $\partial(\omega_d)$ and ω_d:

$$\partial(\omega) = \frac{B_{33}(\omega)}{2(M_f + A_{33}(\omega))} \qquad \omega_d = \sqrt{\omega_0^2 - \partial(\omega_d)^2}$$

$$C_1 = x_0 \quad and\ C_2 = \frac{u_0 + x_0\partial(\omega_d)}{\omega_d}$$

The values used in the equation is given in Table 13 and the solution presented on Figure 44.

Table 13 Parameters used for decay test at Td.

T_d Sec	ω_d Sec^{-1}	$A_{33}(\omega_d)$ Kg	$B_{33}(\omega_d)$ Kg*sec-1	$\delta(\omega_d)$ Sec-1	C1 m	C2 m
4.384	1.433	$1.106*10^5$	$8.962*10^5$	0.12	1	0.084

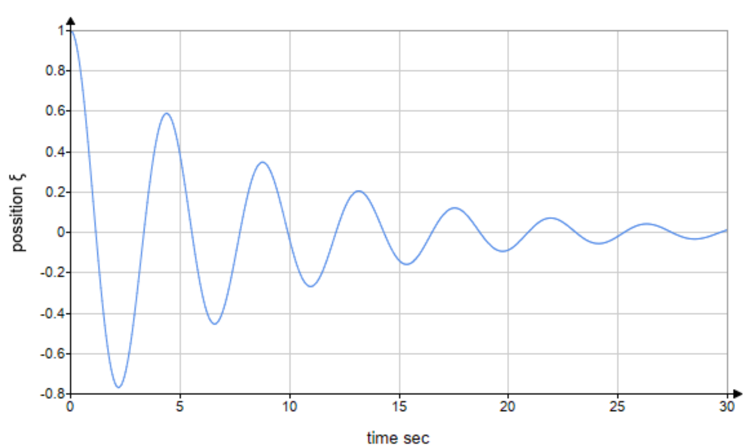

Figure 44 The decay motion calculated.

9.1.4 Forced Oscillation

Considering the case in which the sphere is activated by a vertical wave diffraction force $F_w(t)$ from an incoming sinusoidal water wave of amplitude A, wave period T and with a phase difference Φ_F relative to the wave. From WAMIT we have for the given wave period T the diffraction force coefficient $X_3(T)$ the added mass A_{33} and damping coefficient as well as the phase difference Φ_F

$$F_w = AX_3 \, cos(\omega t + \phi_F)$$

Without external damping $B_{33}^0 = 0 \; and$ without additional external spring $c_{33} = 0$ becomes and restricted to vertical forced motion *j=3 and k =3*, the equation of motion reads:

$$\left(M_f + A_{33}\right)\ddot{\xi_3} + B_{33}\dot{\xi_3} + C_{33}\xi_3 = AX_3 \, cos(\omega t + \phi_F)$$

The solution to this equation describing the position in time is also cosine function $\xi_3(t)$ with amplitude x_0 and a phase difference ϕ_x to the surface wave.

$$\xi_3(t) = x_0 \, cos(\,\omega t + \phi_x)$$

The velocity amplitude u_0 is related to the amplitude of the motion x_0 by $u_0 = \omega x_0$ and a phase difference of $\pi/2$.

$$\dot{\xi_3}(t) = \omega x_0 \, cos(\,\omega t + \phi_x + \frac{\pi}{2})$$

To be a solution to the differential equation the excursion amplitude is given as:

$$x_0 = \frac{A \cdot X_3}{|Z| \cdot \omega} = \frac{A \cdot X_3}{\omega\left[{B_{33}}^2 + (\omega(M_f + A_{33}) - C_{33}/\omega)^2\right]^{1/2}}$$

$|Z|$ is the absolute value of the complex impedance expressed as:

$$|Z| = \left\{{B_{33}}^2 + (\omega(M_f + A_{33}) - C_{33}/\omega)^2\right\}^{1/2}$$

The phase angle between force and velocity is found as:

$$\phi = arctan(\,(\omega(M_f + A_{33}) - C_{33}/\omega)/B_{33})$$

Extending this theory of forced oscillations into problem of the heaving sphere we can compute the response amplitude for the sphere to incoming sinusoidal waves of amplitude A=1m. The phase difference between the wave surface and the position is:

$$\phi_x = \phi_F - \phi - \frac{\pi}{2}$$

Using the frequency dependent exiting force amplitude X_3 and ϕ_F and hydrodynamic coefficients A_{33} and B_{33} are calculated using WAMIT and we get the response curve as indicated on Figure 45

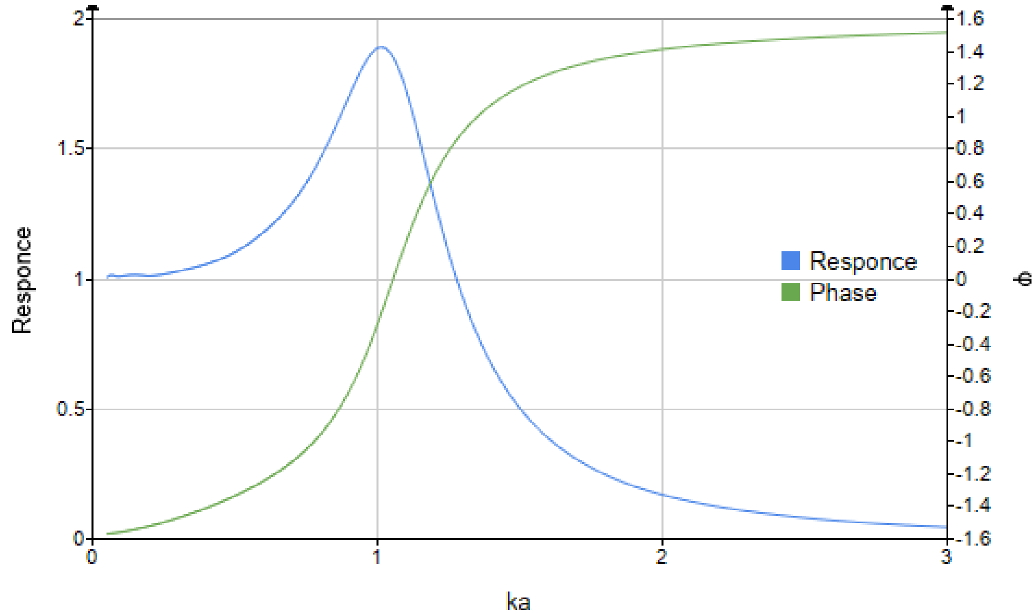

Figure 45 Plot of the response of the sphere to incoming waves

The response of the sphere with no external PTO damping was calculated by the participants for three steepness of regular waves. Participants with non-linear codes obtained noticeable lower RAO at resonance compared to linear sim. The results were presented at a webinar power point 2/28/2017.

T	λ	B_{opt}(T)	B_{33} (T)	A_{33} (T)	X_3(T)
sec	m	kgsec^{-1}	kg sec^{-1}	kg	m^{-2}sec^{-2}
3.0	14.1	3.99×10^5	4.70×10^4	1.03×10^5	9.78×10^4
4.0	25.0	1.19×10^5	8.24×10^4	1.05×10^5	2.00×10^5
4.4	30.2	9.01×10^4	8.98×10^4	1.11×10^5	2.41×10^5
5.0	39.0	1.62×10^5	9.46×10^4	1.22×10^5	3.00×10^5
6.0	56.2	3.23×10^5	9.17×10^4	1.45×10^5	3.87×10^5
7.0	76.5	4.80×10^5	8.06×10^4	1.67×10^5	4.58×10^5
8.0	99.9	6.34×10^5	6.87×10^4	1.84×10^5	5.14×10^5
9.0	126.4	7.85×10^5	5.68×10^4	1.97×10^5	5.57×10^5
10.0	156.1	9.32×10^5	4.65×10^4	2.07×10^5	5.92×10^5
11.0	188.9	1.08×10^6	3.89×10^4	2.16×10^5	6.23×10^5

9.1.5 Energy Extraction and Optimal Damping

To extract energy from the floating sphere, one must imagine a damper fixed between the float and an external reference frame as illustrated in Figure 46. In practice, the damper could be a hydraulic circuit including a hydraulic motor and generator to convert the absorbed power to electricity or it could be a linear electric magnetic generator. In linear theory, the damper is expressed as a coefficient multiplied with the velocity of the float.

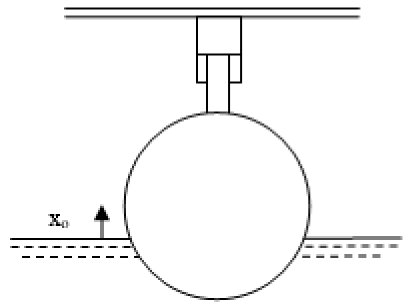

Figure 46 Float connected to external damper.

If the sphere motion is damped by applying an external linear damping force proportional to the velocity by $B_{33}^0(rd)$ the equation of motion for the given wave period T can be written:

$$(M_f + A_{33})\ddot{\xi}_3 + (B_{33} + B_{33}^0(rd))\dot{\xi}_3 + C_{33}\xi_3 = AX_3\, cos(\omega t + \phi_F)$$

In this equation, the damping coefficient $B_{33}^0(rd)$ is expressed using a factor *rd* multiplied with the square root of the sphere mass time the stiffness:

$$B_{33}^0(rd) = rd\sqrt{M_f C_{33}}$$

Similar to the undamped motion the solution to the equation has a similar form in which the position can be expressed as:

$$\xi_3(t) = x_{d0}\, cos(\,\omega t + \phi_x)$$

and the velocity

$$\dot{\xi}_3(t) = u_{d0}\, cos(\,\omega t + \phi_u)$$

The velocity amplitude u_0 is related to the amplitude of the motion x_0 by $u_0 = \omega x_0$ and the phase constants by $\phi_u - \phi_x = \pi/2$. To be a solution to (5) the excursion amplitude is given as:

$$x_0 = \frac{A \cdot X_3}{|Z| \cdot \omega}$$

$$|Z| = \left\{(B_{33} + B_{33}^0(rd))^2 + (\omega(M_f + A_{33}) - C_{33}/\omega)^2\right\}^{1/2}$$

The phase angle between force and velocity is found as:

$$\phi(rd) = arctan(\,(\omega(M_f + A_{33}) - C_{33}/\omega)/(B_{33} + B_{33}^0(rd))$$

|Z| is the absolute value of the complex impedance which can be expressed as:

$$x_{do}(rd) = \frac{A\, X_3}{\omega\left[(B_{33} + B_{33}^0(rd))^2 + (\omega(M_f + A_{33}) - C_{33}/\omega)^2\right]^{1/2}}$$

The phase difference between the wave surface and the position is:

$$\phi_x = \phi_F - \phi - \frac{\pi}{2}$$

Using this information, the float position in relation to the wave elevation and the position of the center of the float can be presented as a function of time with its phase lag compared to the wave elevation at the center of the float *(ϕF(T)* is the phase lag between the wave and the exciting force):

$$z_f(t, rd) = z_d(rd)\, cos\left(\omega(T)t + \phi F(T) - \phi(rd) - \frac{\pi}{2}\right)$$

The OES Task 10 group was tasked with calculating the absorbed power in the regular waves of three different steepness's.

The steepness was defined as s = H/(gT2), and the steepness values of 0.0005, 0.002 and 0.01 were chosen to see whether this would impact the solutions when models other than linear theory were ap-plied. The wave height is given as H.

The average power generated by the float can be expressed as:

$$P_{abs}(rd) = \frac{1}{2} B_{33}^{0}(rd) \cdot \omega^2 \cdot |z_d(rd)|^2$$

The maximum absorbed power for a given wave period *T* can be found by optimizing damping coefficient r_d that provides the maximum power output in each wave period Falnes (2002):

$$B_{opt} = B_{33}\sqrt{1 + \left(\frac{C_{33} - \omega^2\left(M_f + A_{33}\right)}{\omega B_{33}}\right)^2}$$

The optimal damping B_{opt} can be expressed as a damping factor.

$$rd_{opt} = \frac{B_{opt}}{\sqrt{M_f S_b}}$$

The incoming power in the wave of amplitude A is:

$$P_w = \frac{\rho g^2}{32\pi}(2A)^2 T$$

The capture width ratio (CWR) expresses how much power the float absorbs compared to the incoming wave power over its diameter *D*:

$$CWR(rd) = \frac{P_{abs}(rd)}{D \cdot P_w}$$

For point absorbers, Falnes [15] derived the theoretical maximum for resonance absorption as:

$$PAth(T) = \frac{\lambda(T)}{2\pi \cdot D} = \frac{gT^2}{4\pi^2 \cdot D}$$

From Figure 8, one sees that heaving sphere reaches its theoretical maximum CWR at its resonance period, which when inserted in Equation 30 gives *PAth (4.4 sec) = 0.48*.

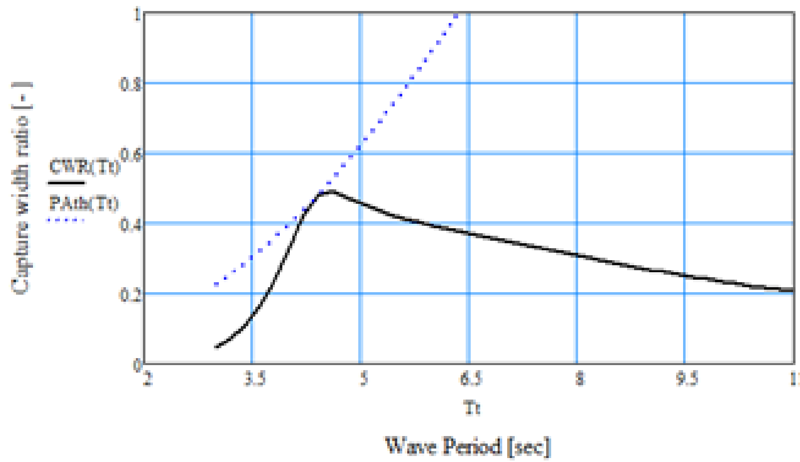

Figure 47 CWR in regular waves

9.1.6 Calculation of Annual Energy Production

To evaluate the energy production from a WEC at a specified site the Capture Length over a range of regular wave periods can be combined with the spectrum of the irregular sea state of specified Hs and Te. The annual energy production calculated following the simplified methodology provided by Nielsen & Pontes (2010) reduces the scatter diagram to the distribution of six sea states and a specified occurrence in hours per year (or %).

P(t) is calculated or measured average power absorption in a regular wave of period t, The capture length L(t) is equal to the power absorbed by the WEC divided by the wave power per meter J(t)

$$L(t) = \frac{P(t)}{J(t)}$$

The results from regular waves to evaluate the absorbed power P in irregular sea state using:

$$P = \int_{0}^{Tmax} S(t)cg(t)\frac{1}{t^2}L(t)dt$$

Table 14 Calculation of the annual energy production at the North Sea site (see table 4)

H_s [m]	1	2	3	4	5	5,5	Ave/sum
Te, [sec]	5,73	6,47	7,22	7,96	8,71	9,08	
Pabs [kW/m]	8,7	37,1	86,6	156,9	246,7	354,1	**54,56**
Hours per year [hours]	3224	2742	1480	631	245	123	8445
Energy per year [kWh/m]	27.984	101.635	128.153	99.026	60.450	43.550	460.798

9.2 THE DTU OWC EXAMPLE

The fourth set of experiments was provided by DTU in Denmark – representing a single OWC chamber mounted on the side of a wave flume, is described in section 6.4. I this section we will provide the theory behind the linear calculations.

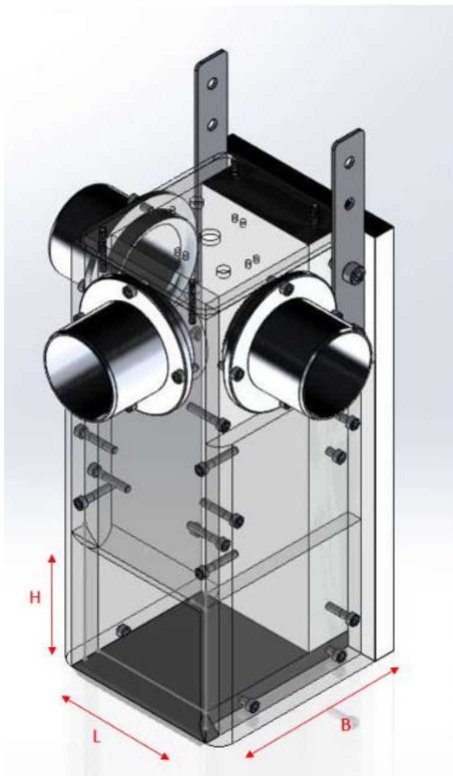

(a) 3D CAD model of the OWC chamber.

(b) Photograph of the OWC chamber in place for tests.

Figure 48 Illustration of the fixed model of the OWC

The equation of motion for a wave energy converter can be described as an oscillating system, activated by the wave excitation force, and damped via the PTO.

The piston mode equation of the fixed OWC can be written as:

$$AX_7 = [-\omega^2 A_{77} + \mathrm{i}\omega(B_{77} + B_{77}^0) + C_{77}]\xi_7$$

Where:

X_7 is the wave diffraction exciting force coefficient.
A is the wave amplitude.
ξ_7 is the vertical response of the water surface “lid”
ω is the angular frequency.
A_{77} added mass.
B_{77} damping coefficient
C_{77} is the hydrostatic restoring coefficient,
B_{77}^0 is the damping from the PTO air-turbine

The equation of motion includes three types of forces.

1 **Inertia**: In the OWC case we have only A_{77} added mass (inertia - in phase with acceleration)

2 **Damping**: In the OWC case we have B_{77} hydrodynamic damping and B_{77}^0 the damping from the PTO air-turbine (– in phase with the velocity). Additional damping could be due to fluid losses related to drag/vorticity/viscosity B_a. Note that the latter fluid losses are very significant in high amplitude responses and are often omitted from simplified models and even when included are not easily linearized (as a result, caution and expert judgement is needed when designing using numerical models based on linear theory). (In phase with velocity)

3 **Stiffness**: In the OWC case we have C_{77} the hydrostatic restoring coefficient. (In phase with position)

The value of the coefficients is depending on the wave period T:

$X_7(T)$ is the diffraction exciting force coefficient.
$A_{77}(T)$ and $B_{77}(T)$ are the radiation added mass and damping coefficient,
C_{77} is the hydrostatic restoring coefficient.
$C_{77} = S_c \rho_w g$ where S_c is the internal free surface of the OWC chamber

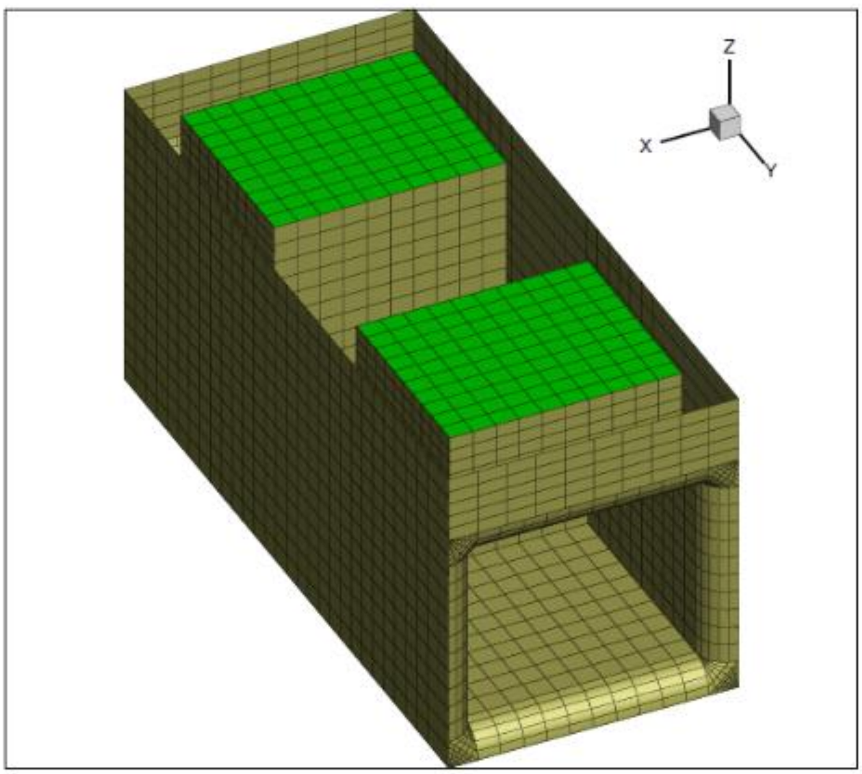

Figure 49 Illustration of the double chamber OWC

The added mass and damping coefficients and the excitation force coefficients are provided in the WAMIT coefficient output files for the double-chamber model with 1 DOF.

The output is non-dimensional and the length scale L=1m, and g=9.81m/sec^2 for these calculations.

$$A_{77}(T) = \overline{A_{77}}(T)\rho L^3$$

$$B_{77}(T) = \overline{B_{77}}(T)\rho\omega L^3$$

$$X_7(T) = \overline{X_7}(T)\rho g L^3$$

$$\varphi(T) = \bar{\varphi}(T) * \pi/180$$

The OWC chamber will respond to the excitation force as a damped Oscillator with impedance Z and the absolute value |Z| of the complex impedance, can be expressed as:

$$|Z| = \{(B_{77} + B_{77}^0)^2 + (\omega A_{77} - C_{77}/\omega)^2\}^{1/2}$$

The *impedance* is composed of two terms *reactance* the *resistance*.

the *reactance* including **mass** and **stiffens.**

$$(\omega A_{77} - C_{77}/\omega)$$

the *resistance* including **damping** terms.

$$(B_{77} + B_{77}^0)$$

The response amplitude ξ_7 of the surface "lid" to the wave excitation force with wave amplitude A and frequency ω can be calculated as:

$$\xi_7 = \frac{AX_7}{|Z|\omega} = \frac{AX_7}{\omega[(B_{77} + B_{77}^0)^2 + (\omega A_{77} - C_{77}/\omega)^2]^{1/2}}$$

The phase angle between force and velocity is found as:

$$\phi = arctan(\,(\omega A_{77} - c_{77}/\omega)/(B_{77} + B_{77}^0)$$

9.2.1 Open Chamber Experiment

The response of the OWC surface with open top (no external damping) $B_{77}^0 = 0$ is calculated for the regular waves. Using the frequency-dependent exciting force amplitude X_7, hydrodynamic coefficients A_{77} and B_{77} calculated using WAMIT inserted into (6), we get the response curve and phase as indicated in Figure 1 as a function of the wave period.

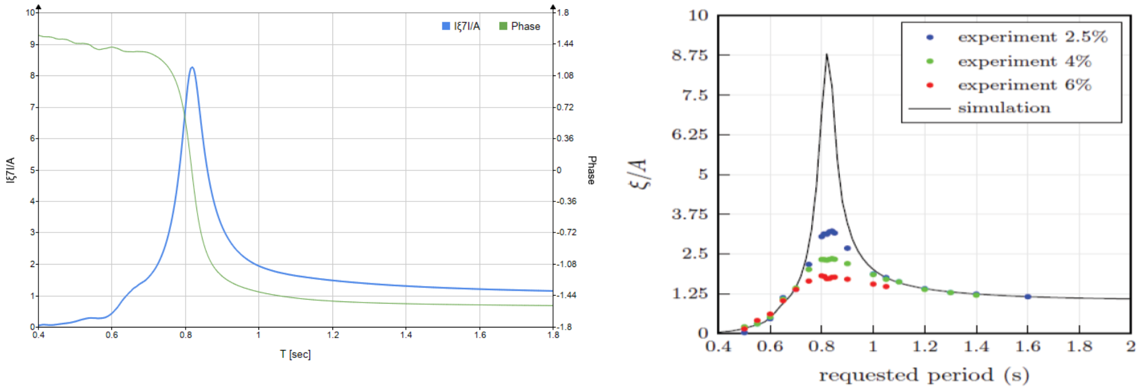

Figure 50 The calculated RAO for the open chamber OWC in full scale and model scale.

9.2.2 Time domain plot

The incoming wave at the center location of the OWC chamber can be described as a sinusoidal wave of amplitude *A* and frequency ω:

$$\eta(t) = A\,cos(\,\omega t)$$

The wave excitation force $F_e(t)$ on the massless surface lid in the form:

$$F_e(t) = AX_7 \cos(\omega t + \phi_F)$$

Where X_7 is the wave excitation coefficient and the phase ϕ_F is the frequency depending on phase difference compared to the phase of the incoming wave. The phase difference between the wave and the force is ϕ_F which is provided by WAMIT. The harmonic time variation of the velocity of the mass-less surface piston with amplitude is calculated from (5) & (6):

$$\dot{\xi}_7(t) = \omega \xi_7\,cos(\,\omega t + \phi_F - \phi)$$

The variation of the position of the lid is π/2 out of phase whit the velocity:

$$\xi_7(t) = \xi_7\,cos(\,\omega t + \phi_F - \phi - \frac{\pi}{2})$$

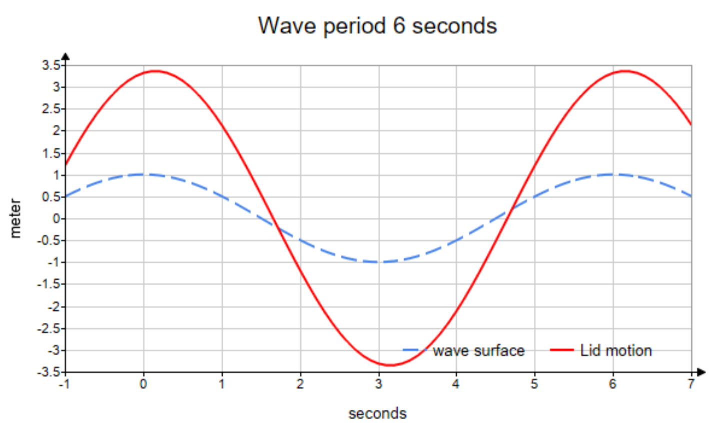

Figure 51 Plot of the wave surface elevation, the OWC surface elevation for T=6 sec no damping

9.2.3 Chamber with an orifice (Damped motion)

If there is an orifice opening in the roof of the chamber, the flow *Q(t)* through the orifice, will be related to the pressure Δ*P(t)* and orifice opening area A_d and the discharge coefficient c_d as:

$$Q(t) = c_d A_d \sqrt{\frac{2}{\rho_a} \Delta P(t)}$$

The pressure drop is related to the flow Q(t) as:

$$\Delta P(t) = \frac{\rho_a}{2} \left[\frac{Q(t)}{c_d A_d}\right]^2 sign\big(Q(t)\big)$$

Assuming incompressibility the flow Q(t) through the orifice is equal to the surface velocity $\dot{\xi}_7(t)$ times surface area S_c of the OWC:

$$Q(t) = S_c \dot{\xi}_7(t)$$

The pressure caused by the flow through the orifice is proportional to the velocity squared and the sign follows the flow direction. This can be written:

$$\Delta P_{NL}(t) = \frac{\rho_a}{2} \left[\frac{1}{c_d} \frac{S_c}{A_d}\right]^2 \dot{\xi}_7(t)^2 sign\left(\dot{\xi}_7(t)\right) = R_0 \dot{\xi}_7(t)^2 sign\left(\dot{\xi}_7(t)\right)$$

The value of R_0 is depending on the surface area and the orifice opening area A_d.

$$R_0 = \frac{\rho_a}{2} \left[\frac{1}{c_d} \frac{S_c}{A_d}\right]^2$$

9.2.4 Linear damping

In the linear case the load from the applied linear PTO damping B^0_{77} times the velocity acts as a force on the piston lid. The pressure in the chamber equals the force divided by the surface area S_c:

$$\Delta P_L(t) = F_d(t)/S_c = \dot{\xi}_7(t) B^0_{77}/S_c$$

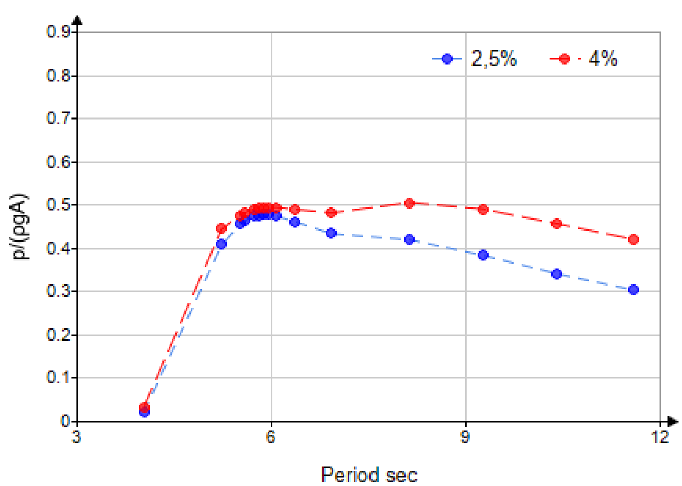

Figure 52 non-dimensional pressure as function of the Wave period.

9.2.5 Linearized nonlinear damping.

Assuming the average absorbed power over one wave period is the same we can find a relation between the linear damping coefficient and the nonlinear orifice damping. By equation the average power absorbed in the linear and nonlinear case we obtain the following relation between the linear damping B_{77}^0 and the orifice damping ration R_o.

$$B_{77}^0 = \frac{8\omega}{3\pi}|\xi_7|S_c R_0 = \frac{16}{3T}|\xi_7|S_c R_0$$

One can see that the linear damping that give the same power as the nonlinear case is proportional to the surface response inversely proportional to the wave period. Since this coefficient is a function of the magnitude of the response, the equations of motion must be solved iteratively at each Wave period and wave steepness A(T).

$$B_{77}^0(rd) = \frac{16}{3T}|rd * A|S_c R_0$$

Starting with an initial value rd=1 for example for a wave period of 6 seconds after a few iterations one will find that rd =1.038 will satisfy:

$$\xi_7(rd) = rd * A$$

The solution to this equation of motion is a harmonic oscillation with the same frequency of oscillation as the applied force. The amplitude of the oscillation can be calculated as:

The response amplitude ξ_7 of the surface "lid" to the wave excitation force with wave amplitude A and frequency ω can be calculated as:

$$\xi_7(rd) = \frac{AX_7}{|Z(rd)|\omega} = \frac{AX_7}{\omega[(B_{77} + B_{77}^0(rd))^2 + (\omega A_{77} - C_{77}/\omega)^2]^{1/2}}$$

The phase angle between force and velocity is found as:

$$\phi(rd) = arctan((\omega A_{77} - c_{77}/\omega)/(B_{77} + B_{77}^0(rd))$$

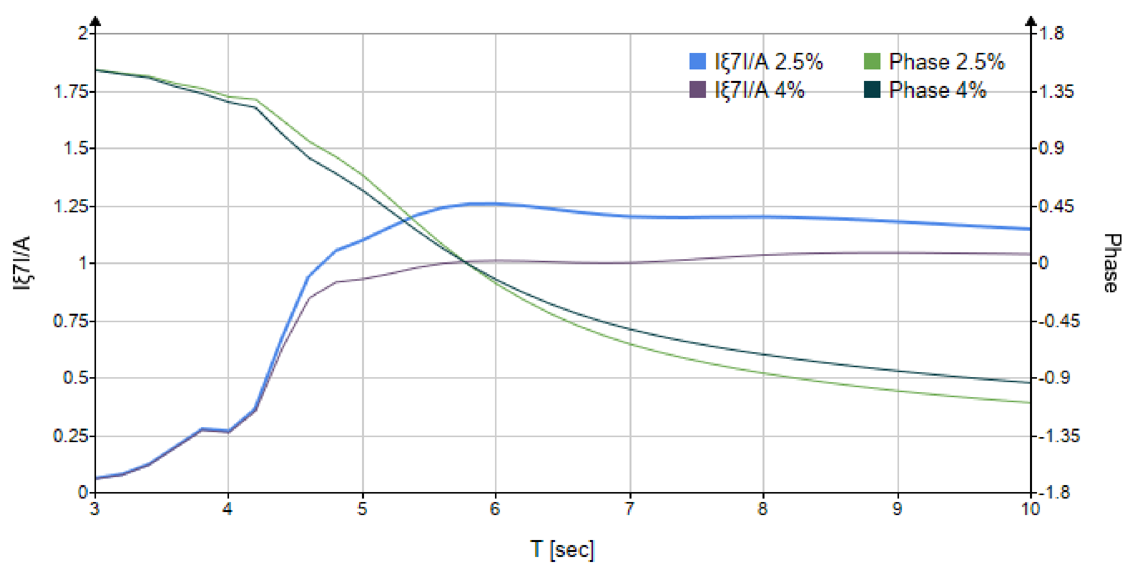

Figure 53 Response and Phase for the damped motion.

9.2.6 Absorbed power and Capture width.

The power generated by the OWC chamber can be expressed as:

$$P_{abs}(t) = Q(t) * \Delta P(t) = S_c \dot{\xi}_7(t) * \dot{\xi}_7(t) B_{77}^0 / S_c$$

$$\dot{\xi}_7 = \omega * \xi_7(rd)$$

The average power generated over a wave period T can be expressed as:

$$P_{abs}(rd) = \frac{1}{2} B_{77}^0(rd) * \omega^2 * |\xi_7(rd)|^2$$

The incoming wave power is

$$P_w(T, H, d) = \frac{\rho g}{8} H^2 cg(T, d)$$

Where $cg(T, d)$ is the group velocity associated with wave period T and depth d.

The calculated CWR for the full scale chamber is shown below using a length scale of L=7.5 meter

$$CWR(T) = \frac{P_{abs}(rd)}{P_w(T, H, d) * 7.5m}$$

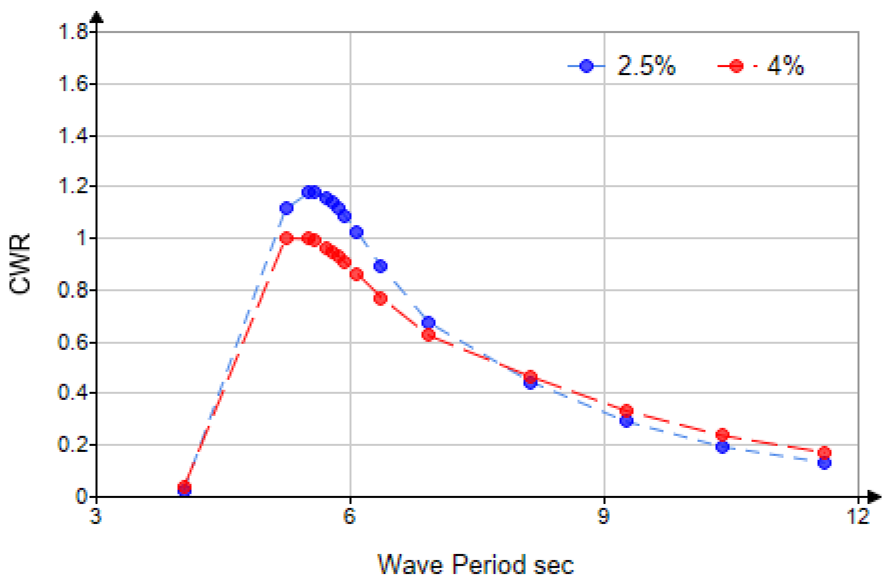

Figure 54 Calculated Capture width ratio for the double chamber OWC as function of wave period.

10 ACKNOWLEDGEMENTS

The work described in this report is the result of dedicated collaboration between researchers from several different countries.

The support from NREL hosting the SharePoint server and their team of dedicated researchers has been the base for security and success. Thanks to Bob Thresher who have attended all webinars over the project period – and providing a personal and warm feedback to the team. Today Toan is the anker man who with dedication and patience manage the information stored, before him Yi-Hsiang Yu still active in OES Task 10, but now in Taiwan, and in the very beginning it was Fabian Went that helped getting the project up and running together with Kelley Ruehl. Today Fabian is working with in Ramboll, Germany,

DTU is the Danish trusted partner with Harry Bingham as the “rock” scientist on hydrodynamics whom with patience and knowledge have made all participating partners feel comfortable sharing results in an open and trustful manner – this is a key aspect for the collaboration, and Harry is supported by Robert Read and Bárður Joensen. Bardur is now working from the University on the Faroe Islands.

AAU has provided dedicated experiments of outstanding quality to the task, led by Morten Kramer, who is not easily impressed unless the experiments can be repeated and show exactly the same results. Morten has been supported by Jacob Andersen and Sarah Thomsen from Floating Power Plant where Morten has his second base. Claes Eskilsson has also assisted working part time at AAU and part time at Rise in Sweden.

KRISO in Korea has supported in providing and assisting in the preparation of experimental data has been greatly appreciated, with a special Thanks to Jeong-Seok Kim, Bo Woo Nam, Kyong-Hwan Kim, Sewan Park, Seung Ho Shin, Keyyong Hong.

The Heaving float test data from the Mask basin was provided by Sandia with the kind assistance from Giorgio Bacelli and Ryan Coe, helping explain the methodology used and uploading and sharing the test data selected.

The experimental DTU OWC model data prepared via several student projects students, thanks to Frederik Pors and Morten Simonsen, Damien Ducasse, Oliver Billeskov, Azin Lamei, Christine Lynggård Hansen, Jacob Suhr, Jokin Brito, Pierpaolo Mauro and Nicolas De Pinho Dias

The list of partners on the OES Task 10 mailing list is long includes 118 names, so the dedicated thanks go to all that over the year has participated, and for me personally it is great honour to have early pioneers now emeritus professors like Tony Lewis from HMRC in Ireland and Spyros Mavrakos from NTUA in Greece join the calls and contribute to the further development of the test cases.

A special thanks goes to the financial support that the project has been given in Denmark, Sweden, USA from DOE via NREL and the Teamer program, and finally the EU funded WECANET for fostering collaboration.

11 REFERENCES

References to information on Numeric models

[1] WAMIT. WAMIT; User Manual, Version 7.0; WAMIT, Inc.: Chestnut Hill, MA, USA, 2008–2012. Available online: http://www.wamit.com

[2] Nemoh 2015 Open source BEM Available: http://openore.org/tag/nemoh/.

[3] OrcaFlex. https://www.orcina.com/SoftwareProducts/OrcaFlex/. Accessed: May 2, 2019.

[4] ANSYS Inc. (2018). Aqwa theory manual 19.1. Technical report.

[5] DSA Ocean (2024). https://dsaocean.com/proteusds/.

[6] WEC-Sim (Wave Energy Converter SIMulator). Available online: https://wec-sim.github.io/WEC-Sim/

[7] Bingham, H.B.; Read, R. DTUMotionSimulator: A Matlab Package for Simulating Linear or Weakly Nonlinear Response of a Floating Structure to OceanWaves. 2020. Available online: https://gitlab.gbar.dtu.dk/oceanwave3d/DTUMotionSimulator

[8] FRyDoM (2024). https://sites.google.com/dice-engineering.com/frydom

[9] Palm, J. & C. Eskilsson (2023). Verification and validation of MoodyMarine: A free simulation tool for modelling moored MRE devices. In Proceedings of the 15th European Wave and Tidal Energy Conference, Bilbao, Spain.

[10] Shipflow software https://www.flowtech.se/

MARIN (2022) Theory documentation DIFFRAC - v3.5.0. "https://www.marin.nl/en/facilities-and-tools/software/diffrac"

OpenCFD (2023) OpenFOAM (open source Field Operation And Manipulation).URL http://www.openfoam.com

IEA, EU and OES references

[11] IEA Wind TCP Task 30 https://iea-wind.org/task30/

[12] Nielsen Kim ANNEX II Development of recommended practices for testing and evaluating ocean energy systems IEA OES 2003

[13] Nielsen, K. and Pontes, T., 2010. Generic and Site-related Wave Energy Data. Report T02-1.1 OES IA Annex II Task 1.1. *(online https://www.ocean-energy-systems.org/publications/oes-reports/guidelines/document/generic-and-site-related-wave-energy-data-2010-/)*

[14] WECANET https://www.wecanet.eu/

[15] Falnes, J. 2002. Ocean waves and oscillating systems. Cambridge University Press.

[16] CoorPower Ocean https://corpowerocean.com/

OES Task 10 references

[17] EWTEC 2017, Wendt, F.; Yu, Y.H.; Nielsen, K.; Ruehl, K.; Bunnik, T.; Touzon, I.; Nam, B.; Kim, J.; Kim, K.H.; Janson, C.; Jakobsen, K.R.; Crowley, S.; Vega, L.; Rajagopalan, K.; Mathai, T.; Greaves, D.; Ransley, E.; Lamont-Kane, P.; Sheng,W.; Costello, R.; Kennedy, B.; Thomas, S.; López, M.; Bingham, H.; Kurniawan, A.; Kramer, M.; Ogden, D.; Girardin, S.; Babarit, A.; Wuillaume, P.Y.; Steinke, D.; Roy, A.; Beatty, S.; Schofield, P.; Jansson, J.; Hoffman, J. International Energy Agency Ocean Energy Systems Task 10 Wave Energy Converter Modeling Verification and Validation. Proceedings of the 12th European Wave and Tidal Energy Conference. 2017

[18] RENEW 2018 Nielsen, K.; Wendt, F.; Yu, Y.; Ruehl, K.; Touzon, I.; Nam, B.; Kim, J.; Kim, K.; Crowley, S.; Sheng, W.; others. OES Task 10 WEC heaving sphere performance modelling verification. Advances in Renewable Energies Offshore: Proceedings of the 3rd International Conference on Renewable Energies Offshore), October 8-10, 2018, Lisbon, Portugal. CRC Press, p. 265.

[19] J. Mar. Sci. Eng. 2019, Wendt, F.; Nielsen, K.; Yu, Y.H.; Bingham, H.B.; Eskilsson, C.; Kramer, M.; Babarit, A.; Bunnik, T. Ocean energy systems wave energy modelling task: Modelling, verification and validation of wave energy converters. J. Mar. Sci. Eng. 2019, 7, 379. [CrossRef]

[20] Energies 14:1718, 2021, Bingham HB, Yu YH, Nielsen K, et al (2021) Ocean Energy Systems wave energy modelling task 10.4: Numerical modelling of a fixed oscillating water column. Energies 14:1718. https://doi.org/10.3390/en14061718

[21] Coe, R.G.; Bacelli, G.; Patterson, D.; Wilson, D.G. Advanced WEC Dynamics & Controls, FY16 Testing Report. Technical Report SAND2016-10094, Sandia National Laboratories, 2016.

[22] Bingham, H.B.; Ducasse, D.; Nielsen, K.; Read, R. Hydrodynamic Analysis of Oscillating Water Column,Wave Energy Devices. J. Ocean Eng. Mar. Energy 2015, 1, 405–419.

[23] 2023 Kilwon Kim, Sewan Park, ChangHyuck Lim, Kyong-Hwan Kim, Seung-Ho Shin The Performance evaluation of 30kW class OWC wave power plant integrated with breakwater, PROCEEDINGS OF THE 15TH EUROPEAN WAVE AND TIDAL ENERGY CONFERENCE, 3–7 SEPTEMBER 2023, BILBAO

[24] Kim Nielsen, Harry Bingham MARINET experiment KNSWING testing an I-Beam OWC attenuator, International Journal of Marine Energy 12 (2015) 21–34

[25] Kramer, M. B., Andersen, J., Thomas, S., Bendixen, F., Bingham, H., Read, R., Holk, N., Ransley, E., Brown, S., Yu, Y-H., Tran, T. T., Davidson, J., Horvath, C., Janson, C. E., Nielsen, K., & Eskilsson, C. (2021). Highly Accurate Experimental Heave Decay Tests with a Floating Sphere: A Public Benchmark Dataset for Model Validation of Fluid-Structure Interaction. Energies, 14(2), [269]. https://doi.org/10.3390/en14020269

[28] Jeong-Seok Kim, Bo Woo Nam, Kyong-Hwan Kim, Sewan Park, Seung Ho Shin, Keyyong Hong, A Numerical Study on Hydrodynamic Performance of an Inclined OWC Wave Energy Converter with Nonlinear Turbine–Chamber Interaction based on 3D Potential Flow, J. Mar. Sci. Eng. 2020, 8, 176; doi:10.3390/jmse8030176

[27] Bingham HB, Joensen B, Read R, Nielsen K, Toan Tran T, Said H A, Kelly T, Ringwood JV, Imai Y, Zanden J, Yu YH, Eskilsson C, Shiri AA, Ocean Energy Systems Wave Energy Modelling Task 10.4: Benchmark Study of the DTU OWC Chamber with One-Way Absorption, Submitted to J. Ocean Engineering and Marine Energy, 06-2024.

[29] Havelock, T. 1955. Waves due to a floating sphere making periodic heaving oscillations. Proceedings of the Royal Society of Mathematics 231(1184). http://rspa.royalsocietypublishing.org/content/231/1184/1

[30] Hulme, A. 1982. The wave forces acting on a floating hemi-sphere undergoing forced periodic oscillations. J. Fluid Mech. 121: 443–463

Books on Hydrodynamics and dedicated on Wave Energy Converters

Newman, J.N. Marine Hydrodynamics; The MIT Press: Cambridge, MA, USA, 1977.

Babarit, A. Wave Energy Conversion. Resource, Technology and Performance; ISTE Press Ltd.: London, UK, 2018.

Cruz, J. Ocean Wave Energy. Current Status and Future Perspectives; Springer: Berlin/Heidelberg, Germany, 2008.

Pecher, A., 2017. Handbook of Ocean Wave Energy. vol. 7. http://refhub.elsevier.com/S0029-8018(24)01919-X/sb32

Folley, M., 2016. Numerical Modelling of Wave Energy Converters: State-Of-The-Art Techniques for Single Devices and Arrays. Academic Press.

Additional WEC and R&D papers

Cummins, W., Iiuhl, W., Uinm, A., 1962. The Impulse Response Function and Ship Motions. Citeseer.

Weber, J. WEC technology readiness and performance matrix - finding the best research technology development trajectory. Proceedings of the 4th International Conference on Ocean Energy, 2012.

P. D. Sclavounos. Nonlinear impulse of ocean waves on floating bodies. J. Fluid Mech., 697:316{335, 2012.

Dallman, A.; Jenne, D.S.; Neary, V.; Driscoll, F.; Thresher, R.; Gunawan, G. Evaluation of performance metrics for the Wave Energy Prize converters tested at 1/20th scale. Renew. Sustain. Energy Rev. 2018, 98, 79–91. [CrossRef]

Jacobsen, N.G.; Fuhrman, D.R.; Fredsøe, J. A wave generation toolbox for the open-source CFD library: OpenFOAM®. Int. J.

Numerical Methods Fluids 2012, 70, 1073–1088. [CrossRef]

Giorgi, G.; Ringwood, J.V. Nonlinear Froude-Krylov and viscous drag representations for wave energy converters in the computation/fidelity continuum. Ocean Engineering 2017, 141, 164–175.

Ransley, E., Greaves, D., Raby, A., Simmonds, D., Hann, M., 2017. Survivability of wave energy converters using CFD. Renew. Energy 109, 235–247.

Heath, T. A review of oscillating water columns. Phil. Trans. Roy. Soc. London A 2012, 370, 235–245.

Vicinanza, D.; Di Lauro, E.; Contestabile, P.; Gisonni, C.; Lara, J.L.; Losada, I.J. Review of innovative harbour breakwaters for wave-energy conversion. J. Waterway, Port, Coastal, Ocean Eng. 2019, 145, 03119001–1–18.

Falcão, A.F.O.; Henriques, J.C.C. Model-prototype similarity of oscillating-water-column wave energy converters. Int. J. Marine Energy 2014, 6, 18–34.